ELSEVIER

Ultramicroscopy 72 (1998) 135–164

ultramicroscopy

The interpretation of HREM images of supported metal catalysts using image simulation: profile view images

S. Bernal, F.J. Botana, J.J. Calvino*, C. López-Cartes, J.A. Pérez-Omil, J.M. Rodríguez-Izquierdo

Departamento de Ciencia de los Materiales e Ingeniería Metalúrgica y Química Inorgánica, Universidad de Cádiz, Apdo 40, Puerto Real, Cadiz 11510, Spain

Received 11 July 1997; received in revised form 20 January 1998

Abstract

The inherent problems of image simulation when applied to the study of supported metal catalysts are analysed and discussed. The paper focuses on the consideration of profile view images with reference to the fine details of the contrasts both in the metal particles and in the outer support layers. As a general conclusion we prove that complex contrasts which very often appear in the images can be interpreted on the grounds of the structural features of the catalysts and on the recording conditions in the microscope. This conclusion is supported by simulation of several experimental images showing excellent fitting with the simulated ones.

One key feature to face for a successful interpretation of metal/support discrete interfaces is the availability of a methodology to construct the complex supercells which are required as input data for the multislice simulation programs. The paper includes a description of the approach followed for this aim in our lab, allowing to model size, shape, faceting, and relative orientation of metal and support particles.

Some other definite aspects addressed specifically in this contribution are: (a) influence of support thickness, (b) influence of the metal particle position on the support, (c) effect of the metal particle size on its visibility and resolution, (d) assessment to the determination of reliable metal particle size by direct measurement from the images, and (e) influence of the crystal tilts in the imaging process. The influence of such variables in the image contrasts are analysed. © 1998 Elsevier Science B.V. All rights reserved.

Keywords: HREM; Supported metal catalysts; Image simulation; Profile views

---

1. Introduction

It is clear from the recent literature that high resolution electron microscopy (HREM) has emerged as a powerful technique for the subnanometric characterisation of different catalytic materials, such as zeolites, oxides, sulphides or oxide-supported metal particles. The publication of several monographic issues [1–5], focused on the application of TEM and, more specifically, HREM to catalysts, should be considered an indication of

---

* Corresponding author. E-mail: solidstate@czv1.uca.es.

PII S0304-3991(98)00009-6

the increasing interest raised by this topic, not only in the field of catalysis but also within the electron microscopy community.

The improvements in resolution achieved in the last decade have allowed micrographs to be recorded in which the structure of very different catalysts is imaged at atomic scale. This very attractive possibility has made HREM a potential source of detailed structural information closely related to macroscopic properties and to inherent catalytic performance.

The continuous lowering of the spatial resolution limit in new equipment demands a parallel effort in the development of interpretation procedures that allow as much structural information as possible to be obtained from the contrasts recorded in the HREM micrographs of this particular type of solid materials. The determination of geometrical features either on real space images or on reciprocal space recordings, such as optical diffractograms or SAED patterns, do not cover all that can be done. In either of these cases, the interpretation of the details of the contrasts contained in the micrographs is disregarded, limiting seriously the quantity and quality of the information that can be extracted from the images. Concerning the field of electron microscopy investigations of supported metal catalysts, the most frequent analysis of the images is the determination of metal particle size distributions. This simple measurement, though being of great interest from the catalytic point of view, does not involve any interpretation of the image contrasts.

As it is well known, the interpretation of HREM image contrasts requires the application of image simulation methods. In fact, this method is routinely employed as a standard procedure to interpretate HREM images of semiconductors, ceramics or intermetallics, among others [6]. Comparing experimental and calculated images, very accurate information has been obtained from a variety of defect structures present in these materials, like point defects, precipitates, interfaces and grain or phase boundaries. Nevertheless, and in spite of the proven interest of image simulation methods, their use in the field of catalytic materials has not been widespread until now. In fact, only a scarce number of papers can be found in the literature where simulated images are carefully analysed to correlate image contrasts with specific, fine detail, structural features of catalysts or catalyst components as is the case of small metal particles. References [7–17] can be considered as representative examples of these works. Most of these contributions deal with the structure of isolated small model metal [9–16] or oxide/sulfide particles [7,13,17]. In any case, until now, a systematic application of image simulation techniques to HREM images of catalysts in general and, in particular, to supported metal catalysts, has not been a common practice.

The unavailability of a widely applicable software designed to build easily the complex supercells necessary to account for models of interest in catalysis, as well as the particularly poor definition in catalytic samples of several fundamental parameters of the imaging process, like crystal orientation and thickness, make image simulation on these materials a difficult task. This could explain the lack of calculated images in most of the published papers dealing with the HREM characterisation of catalysts.

During the last years our group has worked in order to overcome some of the problems cited above and to potentate the use of image simulation techniques in the interpretation of HREM images of catalysts, in general, and of metal/support systems in particular. Thus, we have developed a set of supercell modelling tools that allow to take into consideration the specific features of catalytic samples. These tools have been gathered within the frame of a FORTRAN 77 coded program we have called RHODIUS [18]. The supercells generated by this program can be used as input to the multislice routines of currently available image simulation packages like EMS by P. Stadelmann [19].

In previous works [20–27], following an approach based on calculated images, we have interpreted in detail the nanostructural features of HREM images recorded on several metal/support catalysts like Rh/TiO_2, Rh/CeO_2 or Pt/CeO_2. Very precise information about the specific origin and nature of metal-support interaction effects, hardly accessible by other characterisation techniques, have been drawn. Now, in this paper, we focus the attention on the application of Image Simulation as a tool to understand the influence of the structural parameters specific to supported metal catalysts, on their HREM images. The fundamental features of the interaction between the electron beam and the catalyst have been considered. Topics like (a) the effect of the metal particle position on the support surface, (b) the evaluation of the detection limit of small particles using quantitative criteria and (c) the influence of small crystal tilts, are addressed. Though they will not be considered here, many other structural features, like metal particle shape, metal/support orientation relationships or the chemical nature of support surface, can be investigated using this approach [22]. After this, the limitations of HREM imaging in establishing these parameters can reasonably be accessed on the grounds of the results of these calculations. In any case, the interpretation of the different experimental images discussed in this paper will show how these aspects can be properly treated. In fact, image simulation should be considered as a test bench where an a priori knowledge of image formation of catalytic systems and of the capabilities of HREM in the determination of certain structural features of such materials can be predicted. Moreover, but no less important, image simulation constitutes the only reliable tool to discriminate between real structural features and image artefacts not related to the catalyst's structure. Different examples in connection with these ideas will also be shown in this contribution.

The low magnification image in Fig. 1, recorded on a Rh/CeO_2 catalyst, can be used to illustrate the main distinctive features of metal/support systems. As can be observed, in these materials the metal phase is present as small particles, usually in the nanometer size range, sitting on the surface of larger, micron sized, support crystallites. Two different types of recordings can be obtained in these samples: profile view images, like that exemplified by the metal particle indicated by a black arrow in Fig. 1, and planar view images, as is the case of the particle marked with a white arrow. In the first case the electron beam runs ideally parallel to the contact plane between the metal and the support, in such a way that the metal/support interface is imaged in cross section. As a consequence, in this projection mode the structure of the metal and that

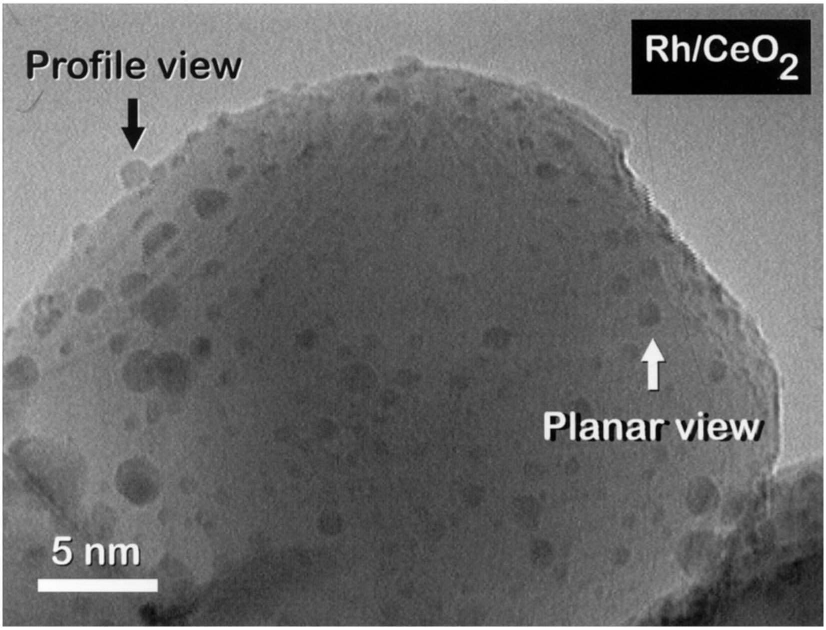

Fig. 1. Low magnification image corresponding to a 2.5% Rh/CeO_2 catalyst.

of the support are imaged in different locations of the micrograph. This neatly contrasts with planar view recordings, where the metal particles are imaged on the support background. In this work we will focus on the study of images recorded in profile view conditions. The analysis of planar view imaging can be also fruitfully exploited, and will be the subject of a future contribution.

2. Experimental details

The experimental HREM images presented in this work have been obtained on two different catalysts: 2.5% Rh/CeO_2 and 4% Pt/CeO_2. Further details concerning the preparation and activation procedures of these catalysts can be found elsewhere [21,25]. Images have been recorded in a JEOL 2000EX microscope equipped with a top entry sample holder and ion pumping. The point resolution attainable with this microscope is 0.21 nm.

All the supercells employed as input models for the image simulations have been modelled using the RHODIUS program developed in our lab. HREM image calculation was performed using the Multislice routines of the EMS package [19] running on an Indy 4400SC Silicon Graphics Workstation.

A conventional CCD camera, with a resolution of 768 × 512 pixels, has been used to digitise the micrographs. Image processing of these digital images has been performed using the PC version of SEMPER 6+ software by Synoptics.

3. Preliminary considerations and definitions

Prior to describing any result it is convenient to consider briefly the different features of the image simulation process which are specific to the materials considered in this study. In relation to this it is important to realise that the simulation of HREM images of supported metal catalysts should be considered as a particular case of simulation of interfaces. In fact, these materials can be simply described as biphasic systems with spatially discrete interfaces. Profile views would correspond to cross section images of these nano-sized interfaces.

In the case of extended interfaces it is well known that to define their structure it is necessary to determine: (1) the structure relationship existing between the two bulk components of the interface. This can be achieved by specifying the zone axes of observation of the two bulk components and the Miller indices of the planes contacting at the interface; (2) the chemical nature of the interface; and, finally, (3) the local atomic displacements from the bulk structure taking place in the interface region. Once the interface has been characterised from the structural point of view, and assuming as fixed the electron-optical properties of the microscope (Cs, defocus spread and beam semiconvergence), to obtain calculated images it is also necessary to fix simulation parameters like thickness (t) and defocus (Δf).

Fig. 2 shows an example of a supercell where an extended $Rh\|CeO_2$ interface is modelled. The z-axis of the supercell has been aligned in this case with the [1 1 0] directions of both components, which are contacting along their $(1\,\bar{1}\,1)$ planes. An oxygen termination for the ceria surface, a distance of 0.156 nm between the Rh and O planes, and no atomic displacement from the bulk positions have been considered in this model. With supercells like this, simulation maps that consider thickness and defocus as variables can be obtained allowing the interpretation of HREM images of extended interfaces.

In the case of supported metal particles, the structure of their interface with the support can be described using the same set of parameters employed in extended interfaces, but to perform image calculation some additional structural and simulation parameters have to be defined. The shape of the metal particle appears as a new structural parameter to be established. In relation to the thickness of the specimen, two variables have to be defined: the support thickness (t) and the metal particle size (d). The position of the metal particle on the support surface (p) appears also as a new simulation parameter. As depicted in Fig. 3, the value of p indicates the distance from the centre of the metal particle to the support exit surface, measured along the direction of the incoming electron beam.

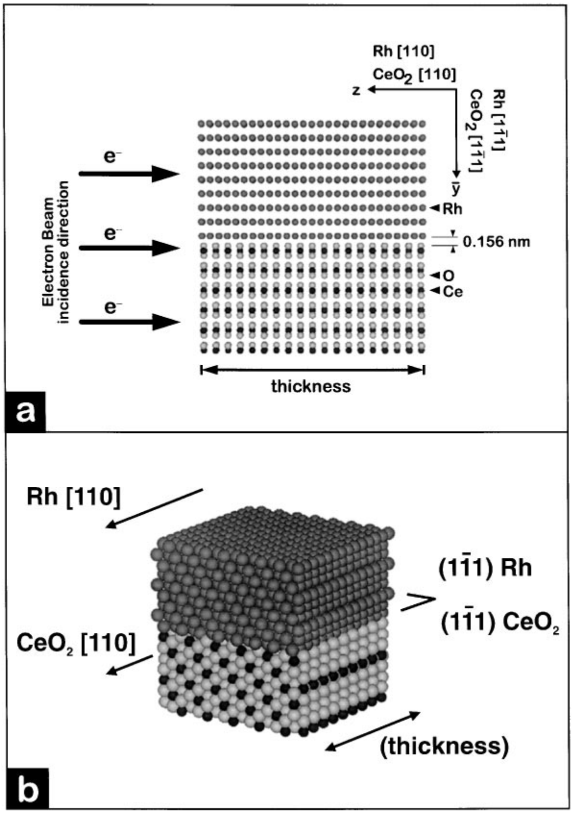

Fig. 2. Projection (a) and perspective (b) views showing a model of a Rh‖CeO$_2$ extended interface.

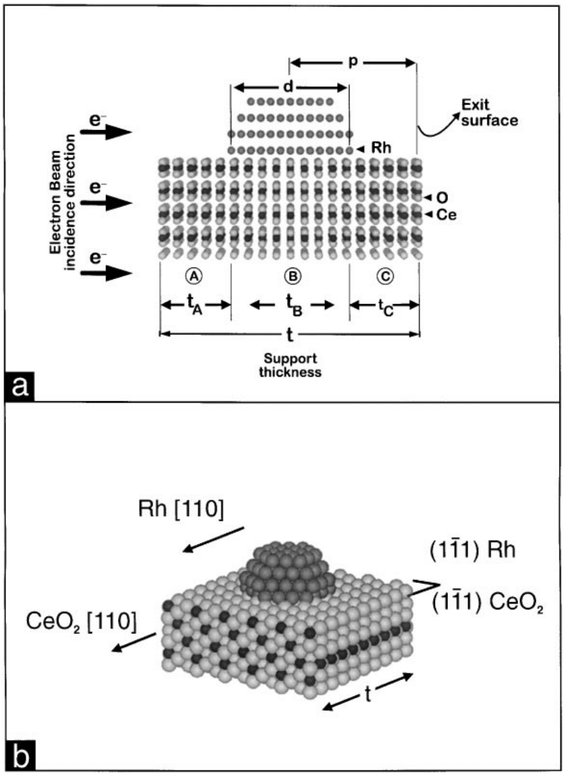

Fig. 3. Projection (a) and perspective (b) views showing a model of a Rh‖CeO$_2$ discrete interface. The structural parameters of the interface are the same as those corresponding to Fig. 2. The parameters, *d*, *t* and *p* have been marked. The shape of the rhodium particle corresponds to a (1 $\bar{1}$ 1) truncated cuboctahedron.

Simulation of metal/support systems have to deal with all the parameters described above: those characteristic of extended interfaces (structural and electronoptical) and those which are specific to this type of problem (shape, *d*, *t* and *p*).

4. Amplitude/phase diagrams in supported metal catalysts

The increase in the number of simulation parameters complicates further the interpretation of HREM images of supported metal catalysts. For this reason, an apriori knowledge of the basic features of the interaction between the electron beam and this type of catalyst sample seems to be suitable, in order to simplify as much as possible the Image Simulation process. This approach has been already used by Glaisher et al. [28–30] in the study of different semiconductors by HREM. In these papers, the evolution of the amplitude and phase of the transmitted and diffracted beams, as a function of crystal thickness, are fruitfully used to interpretate the contrasts of HREM images of those materials in terms of their crystal structure. The rest of this section is addressed to establishing these amplitude/phase curves for supported metal catalysts and to discuss their main features. Though a Rh/CeO$_2$ system in [1 1 0] projection is considered as a study case, the conclusions drawn from this section should be considered of general application and, in all cases, they describe properly the general features of the interaction of the electron beam with metal/support systems.

As sketched in Fig. 3a, the interaction of the electron beam with metal/support systems takes place following three consecutive steps. First there is an interaction of the electron beam with the support component, along the region marked as A. Then, the wave front coming out of A enters a second section, labelled B, where a simultaneous interaction with both the metal particle and the support material takes place. Finally, the electron beam crosses the region C where, again, the interaction takes place only with the support. From now on, the values of the parameters t_A, t_B and t_C, will designate the thickness of regions A, B and C, respectively. The following simple relationships between these parameters and the fundamental simulation parameters can be easily established:

$$d = t_B, \tag{1}$$

$$t = t_A + t_B + t_C, \tag{2}$$

$$p = t_C + \tfrac{1}{2}t_B. \tag{3}$$

Thus, calculating the evolution of amplitudes and phases of the different beams along these three segments it would be possible to rationalise the influence of the simulation parameters (d, t, p) on HREM images of supported metal catalysts. To analyse the specific influence of simulation parameters all the structural parameters have been fixed. For this reason a calculation based on a particular rhodium supported on ceria model, with structural features typical of experimental HREM images recorded on this system [21], has been done. It should be emphasised anyway that any other model with a different structure can be used as the starting point for this calculation. The comparison of calculations corresponding to different models could be used to sort out the influence of the structure on the amplitude/phase diagrams, though this aspect will not be considered here.

In particular, a supercell containing a rhodium particle sitting with one of its (1 1 1) faces on a (1 1 1) ceria surface has been employed. A parallel topotaxy, defined by the crystallographic Eqs. (4) and (5), has been assumed as orientation relationship between Rh and ceria. All these are the most common features experimentally observed in HREM images of this system [21].

$$[1\,1\,0]\mathrm{Rh} \| [1\,1\,0]\mathrm{CeO_2}, \tag{4}$$

$$(1\,\bar{1}\,1)\mathrm{Rh} \| (1\,\bar{1}\,1)\mathrm{CeO_2}. \tag{5}$$

To reduce the computing time and the data storage demand during the calculation, the morphology imposed on the metal particle was that of a hexagonal prism. This morphology has the advantage that its projection along the [1 1 0] direction is the same as that of a truncated cuboctahedron, which is the most common faceting for Rh clusters on ceria [21]. Nevertheless, calculations with any other metal particle morphology can be carried out in a parallel way.

To perform the multislice calculation on the above cited model two different types of slices have to be used, one containing only ceria in [1 1 0] projection, from now on referred to as the S slice, and a second one containing rhodium and ceria, also in [1 1 0] projection, here named the M slice. Fig. 4 shows the supercells corresponding to these two slices built with the RHODIUS program. By stacking these slices in appropriate sequence the interaction of the electron beam with a supported metal particle can be studied using a multislice calculation routine. The interaction along regions A or C would correspond to propagation through slices of the S type, while the interaction in the B region can be simulated using M slices. The values of d, t and p (or the equivalent set of parameters t_A, t_B and t_C) can be easily adjusted by changing the relative number of the two types of slices stacked to build up the whole supercell.

The dimensions of the S and M slices can not be arbitrarily fixed. In order to generate a crystalline material by the stacking procedure it is necessary that they have a thickness, i.e. a Z-axis supercell length, which is an integer multiple of the shortest translation distance along the stacking direction, the [1 1 0] vector of Rh or CeO_2. In the case of the S slice, taking into account that cerium dioxide presents a fluorite unit cell, this condition can be completely fulfilled by choosing as slice thickness the value of its (1 1 0) plane's d-spacing. This corresponds to a slice thickness of 0.383 nm. By stacking a specific number of S slices with this thickness, or

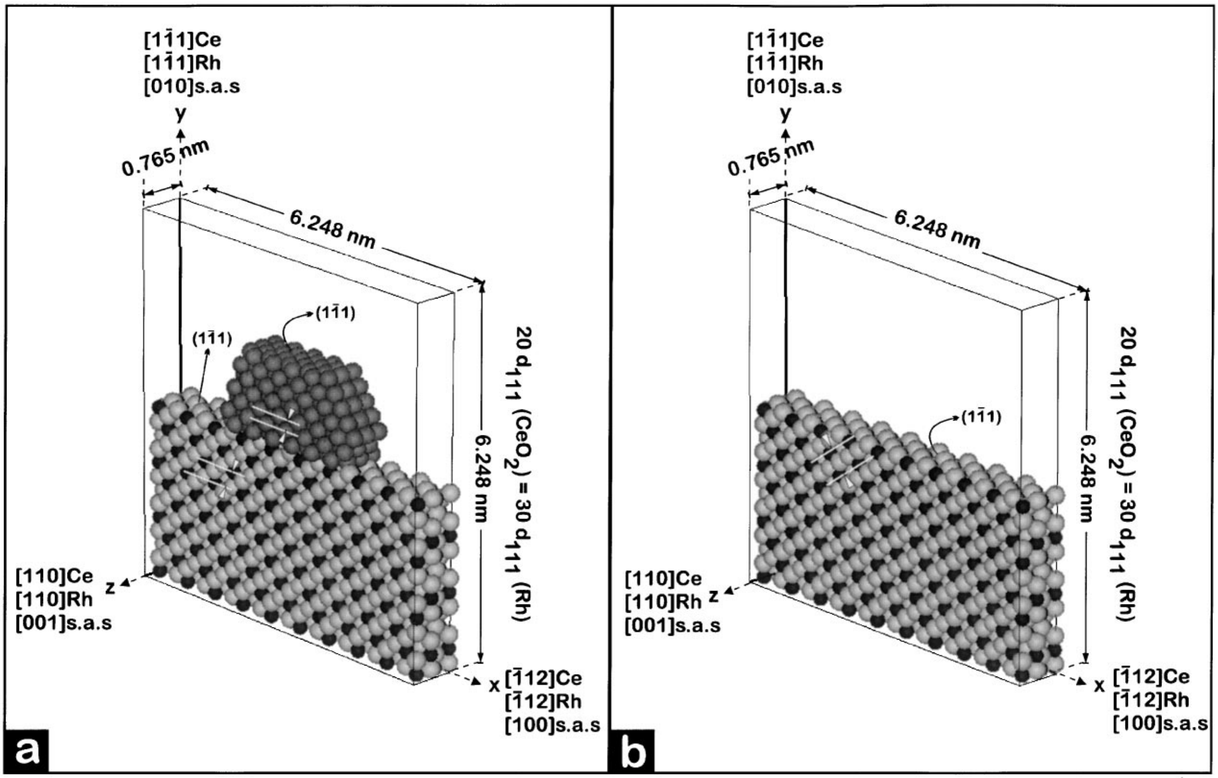

Fig. 4. Structural models of the M (a) and S (b) slices. The dimensions and crystallographic features of these slices are indicated.

an integer multiple of this thickness, zones A or C of Rh/CeO_2 supercells can be modelled.

The case of the M slice is a bit more complicated. For this slice we have to choose a thickness value that accomplishes, simultaneously, the requirement of periodic continuation for two materials with different crystallographic parameters, Rh and ceria. This difficulty can be solved by choosing as thickness of the slice the least common multiple (l.c.m.) between the *d*-spacing of the (1 1 0) planes of the metal and the support. To get such an l.c.m. value it is necessary that the ratio between the (1 1 0) *d*-spacing of the metal and the support can be expressed as a ratio of integer numbers; in other words these values should be commensurate with each other. Given that the values involved in this case are 0.269 nm for d_{110} Rh and 0.383, for d_{110} CeO_2, it is clear that a small distortion in the structure of either the metal or the support needs to be introduced to achieve the required numerical condition. In relation to this point it should be considered that some authors [11,31] have reported the occurrence of distortions (up to 5%) in the lattice parameter of small clusters supported on crystalline oxides. Therefore, it seems reasonable to choose the metal phase as the component to suffer the structural distortion. In the Metal/Support system here considered by decreasing the value of the lattice parameter of rhodium by only 5% the following relationship between the d_{110} spacing of metal and support is established:

$$3d_{110}\mathrm{Rh} = 2d_{110}\mathrm{CeO_2} = 0.765\ \mathrm{nm}. \qquad (6)$$

Taking into account the considerations explained above, a thickness of 0.765 nm was chosen for both the S and the M slices. In this way the calculation requirements are fulfilled while, at the same time, using a model that resembles much closer the currently available experimental data. In any case it is not reasonable to expect extreme deviations in the results with respect to those corresponding to a model containing a non-distorted metal particle. To check this point, different calculations performed on models containing only rhodium with slightly different cell parameters have been performed. The results indicate that no significant modification takes place in the corresponding amplitude/phase curves.

The Y dimension of the slices has also to be adequately fixed. In this respect, and assuming that the $(1\,\bar{1}\,1)$ reciprocal vector has been aligned with the Y axis of the supercell, as sketched in Fig. 4, it is important to note that the length of this axis should be a multiple of the l.c.m. value between the d_{111} spacing of rhodium and CeO_2. Only in this way it is possible to assign integer Miller indices to the $(1\,\bar{1}\,1)$ reflections of both the metal particle and the support with respect to the supercell axis system (s.a.s). For instance, if we choose an Y axis of 6.248 nm length, the indices corresponding to the $(1\,\bar{1}\,1)$ reflections of Rh and ceria, would be the following:

$$g_{1\bar{1}1}(\mathrm{CeO_2}) = g_{0,20,0}(\mathrm{s.a.s}), \tag{7}$$

$$g_{1\bar{1}1}(\mathrm{Rh}) = g_{0,30,0}(\mathrm{s.a.s}). \tag{8}$$

In other words, the evolution of the amplitude and phase of the (0 20 0) reflection of the supercell would correspond to that of the $(1\,\bar{1}\,1)$ planes of ceria and, likewise, the (0 30 0) reflection would account for the $(1\,\bar{1}\,1)$ reflection of rhodium.

Taking into account the arguments stated in the previous paragraphs, the final dimensions of both the S and M slices used for the calculation of the Amplitude/Phase diagrams were 6.248 nm × 6.248 nm × 0.765 nm. A supercell was built by stacking 11 S slices, followed by 4 M slices and ending with another 11 S slices. This 11/4/11 stacking sequence allows to model a Rh/CeO_2 system containing a support crystal with a thickness (t) of 19.9 nm and a small particle with a diameter (d) of 3.1 nm, allocated at 9.9 nm from the support exit surface (p), Fig. 5a.

Figs. 6a and 6b show the calculated amplitude/phase diagrams corresponding to this structural model considering an incident electron beam of 200 kV. Regarding the behaviour of the $(1\,\bar{1}\,1)$ beams for ceria, Fig. 6a, both their amplitude and phase follow the trend observed for bulk ceria. The presence of the metal cluster on top of the ceria surface does not influence significantly the evolution of the diffraction process within the support material.

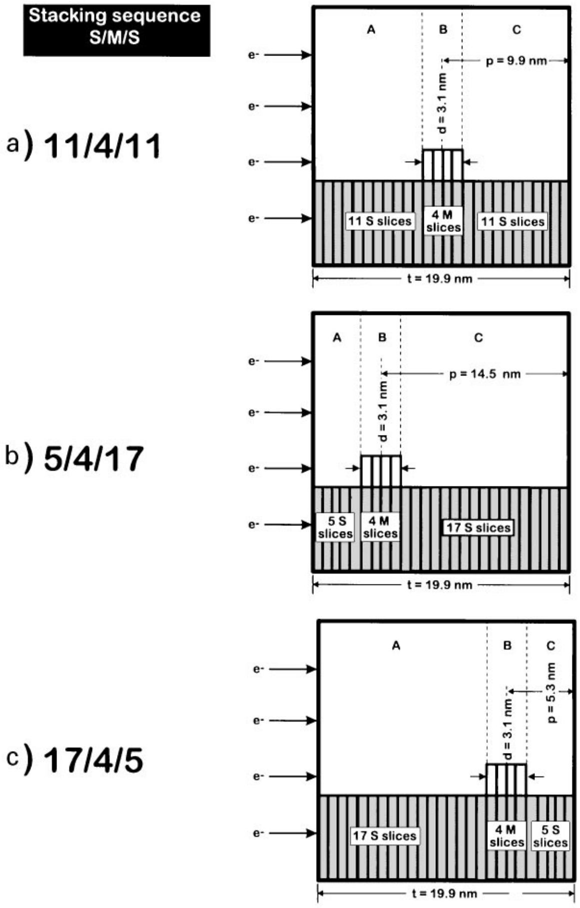

Fig. 5. Schemes of the S/M/S stacking sequences employed to build the three different Rh/CeO_2 supercells employed to calculate the amplitude/phase diagrams. A, B and C correspond to the three different electron beam–sample interaction regions described in the text. Values of d, t and p for each model are indicated.

The evolution of the $(1\,\bar{1}\,1)$ beams of the metal is clearly different. As can be observed in Fig. 6b, there is no intensity within these beams along the A region, then there is a continuous increase in

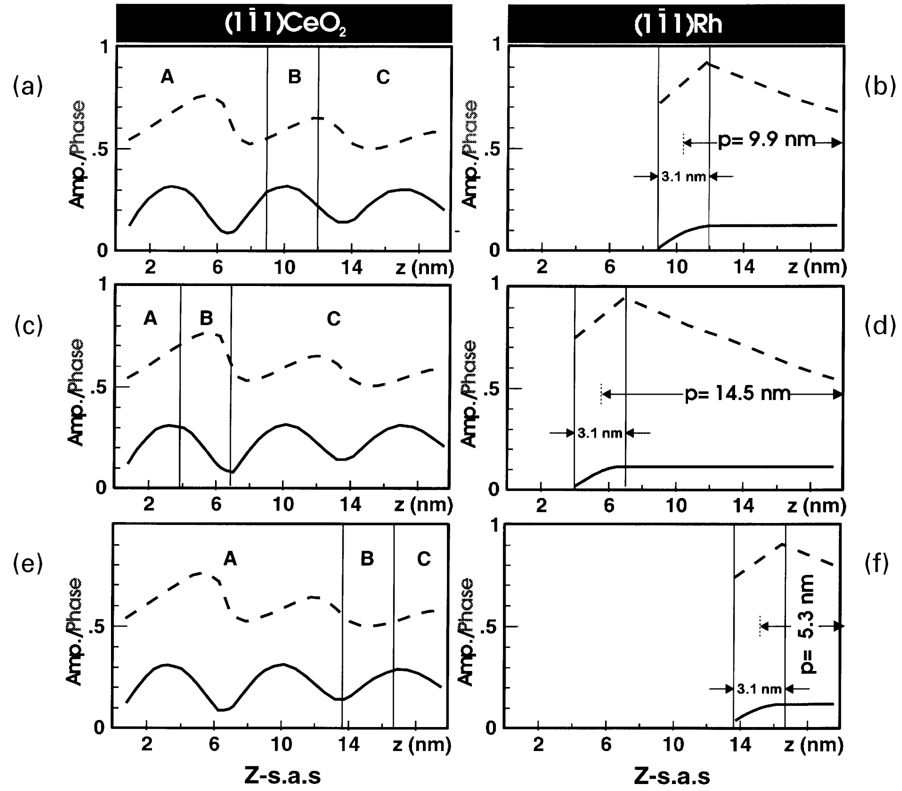

Fig. 6. Amplitude (solid line)/phase (dashed line) diagrams calculated for the (1 1̄ 1) beams of ceria and rhodium. The metal particle is positioned at 9.9, 14.5 and 5.3 nm from the exit surface. The supercells shown in Fig. 5 were used as models for these calculations.

amplitude while the electrons are crossing the metal particle, region B, a maximum diffracted amplitude being reached at the point where the beam leaves the metal particle. From this point on, region C, an amplitude plateau is observed extending up to the exit surface of the supercell. This result indicates that the behaviour of the metal beams depend only on the interaction of the electrons with the structure of the metal particle, at least for a system with the dimensions considered in this calculation. In effect, the absence of intensity in the A region and the steady value observed in C indicate that no significant intensity is being brought into the metal beams from the beams diffracted by the support and, reciprocally, that no intensity from the metal beams is scattered into the support.

Due to their small scattering angle (approx. 2 mrad for 200 kV electrons), it is necessary that the (1 1̄ 1) beams coming out of the metal particle, at a mean distance from the surface of several angstroms, travel a long path before reaching the ceria surface, where they could be further scattered. This argument could explain the results observed above. Additionally, and using the same idea, if the thickness of the ceria support crystallite was large enough it should be expected that this secondary diffraction process would take place. Such interaction should translate into a modification of the amplitude of the metal diffracted beams during their propagation within the support crystallite. Fig. 7 shows the evolution of the Amplitude of (1 1̄ 1) beams of Rh and ceria for a model where a much thicker ceria crystal, 62 nm, has been considered. In this case, although the amplitude of the (1 1̄ 1) beams of rhodium is also nearly constant after exiting the metal particle, with a value close to

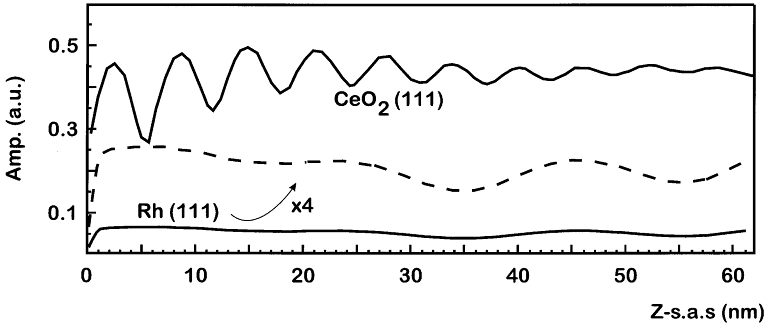

Fig. 7. Amplitude of the (1 $\bar{1}$ 1) beams of rhodium and ceria calculated for a Rh/CeO$_2$ supercell containing a rhodium particle supported on a thick, 62 nm, ceria crystallite. Note in the 4-fold enlargement the fluctuations in the amplitude of the (1 $\bar{1}$ 1) beams of Rh at distances further than 25 nm.

that observed in Fig. 6b, a slight wavy behaviour is evident at large distances. In effect, in the 4-fold enlargement included in the figure, modulations in the amplitude of the (1 $\bar{1}$ 1) beams are clearly evident. Such modulations start to be significant at support thickness greater than 25 nm. At lower values an amplitude plateau is still observed, consistently with that reported in the calculations included in Fig. 6. This result confirms that under specific circumstances, like that considered in Fig. 7, a secondary diffraction process within the support affects the behaviour of the (1 $\bar{1}$ 1) beams of the metal particle.

The evolution of the phase of the metal (1 $\bar{1}$ 1) beams contrasts with that observed for their amplitude. Thus, as shown in Fig. 6b, there is a sharp increase of their phase while the electrons are crossing the metal but once the electrons leave the small particle, a linear decrease takes place, instead of the steady value behaviour observed for their amplitude. A decrease rate, R_{Φ}, around 0.18 rad nm^{-1} can be estimated from Fig. 6b. As it will be further stated, this result has a strong influence on the transfer of the metal particle contrasts into the final image, whose effective defocus will depend strongly on both this phase decrease rate, R_{Φ}, and the actual position of the metal particle on the support surface. The value of this decrease rate of the phase shift between the metal (1 $\bar{1}$ 1) beams and the unscattered central beam is related to the diffraction angle existing between them. In fact the observed value of R_{Φ} can be calculated, in accordance with this idea, using the following equation:

$$R_{\Phi} = \pi \lambda g^2, (\text{rad nm}^{-1}), \tag{9}$$

where g stands for the module of the reciprocal (1 $\bar{1}$ 1) vector of the metal structure (4.56 nm^{-1}) and λ corresponds to the wavelength of 200 kV electrons (0.00251 nm). Using Eq. (8), the total phase shift change along a beam path of value Δp (nm) should be

$$\Delta\phi = R_{\phi}\Delta p. \tag{10}$$

According to these results the beams contributing to the synthesis of the metal image are not greatly influenced by the presence of a thin support crystallite. Although for thick support crystal a slight perturbation of the metal beams' amplitude occurs, the most important effect that influences these beams, once they come out of the metal particle, is the change in their phase as a consequence of free propagation in space.

The influence of the parameter p, the position of the metal particle on the support surface, has also been analysed. For this purpose two additional models have been built and their amplitude/phase diagrams calculated. In these new models the values of t and d where the same as those in Fig. 5a and the value of p was changed. In one of the new models, Fig. 5b, based on a stacking sequence 5/4/17, p is equal to 14.5 nm and in the second, Fig. 5c, based on a 17/4/5 scheme, the value of p was 4.3 nm. Figs. 6c–6f show the results corresponding to the calculation of amplitude/phase diagrams for these two new models. From the analysis of these figures several conclusions can be drawn. First, the position of the metal particle has no influence on the diffraction process in the support. No appreciable change was observed either in the amplitude or the phase of the $(1\,\bar{1}\,1)$ beams of ceria. From these results it can be concluded that the values of these magnitudes depend only on the support thickness (*t*). Regarding with the $(1\,\bar{1}\,1)$ diffracted beams of rhodium, a behaviour similar to that depicted in Fig. 6b is observed. With respect to their amplitude, given that the particle size in these new models has not been changed, the same maximum value is observed at the end of the metal particle. Their phase also shows a similar trend, but the change in the position of the metal particle gives rise to a different value of this parameter at the exit surface of the model. In summary, the position of the metal particle seems to affect selectively the value of the outcoming phase of the metal particle diffracted beams. As will be shown in the next section, this result has a strong influence during the imaging process at the objective lens.

5. HREM simulated images in a Rh/CeO$_2$ catalyst

The calculation of amplitude/phase diagrams provides the main features of the interaction of the electron beam with the supported metal catalyst, nevertheless to fully understand the influence of the structural and imaging parameters, simulated images have to be obtained. Calculations based on different sets of starting Rh/CeO$_2$ supercell models have been performed in order to sort out the role of each of the above cited parameters. The electron-optical values of a JEOL2000EX microscope have been employed for these calculations, Table 1.

5.1. *Effect of support thickness t*

Fig. 8 shows images calculated at 50 and 70 nm defocus, corresponding to a set of Rh/CeO$_2$ supercells where support thicknesses (t) ranging between 3 and 15 nm have been considered. In all cases a $(1\,\bar{1}\,1)$-truncated cuboctahedron rhodium crystallite of 2.2 nm of diameter (*d*), epitaxially grown on a $(1\,\bar{1}\,1)$ ceria surface, at a distance (*p*) of 1.1 nm from the exit surface has been considered, Fig. 9.

The comparison of images calculated at the same defocus indicates that the change in image contrasts in the support region due to thickness changes does not influence at all the contrasts observed in the metal particle, except at the zones very close to the interface, where only very tiny modifications take place. In fact the contrasts observed in the support are the same as those observed for bulk ceria and those in the particles the same as those seen for isolated, unsupported, rhodium metal

Table 1
Electronoptical parameters of different HREM microscopes

Microscope	A_p^a (nm^{-1})	HV^b (kV)	C_s^c (mm)	C_c^c (mm)	Δ (nm)	θ (mrad)	Δf_0^d (nm)	Δf_2^e (nm)	Resolution^{c,f} (Å)
JEOL 2000EX^g	10	200	0.7	1.2	10	1.2	51	98	2.1
JEOL 2010F	12	200	0.5	1.0	3	1.0^h	43	83	1.9
Philips CM30/T	10	300	2.0	2.0	8	1.0^h	77	147	2.3
JEOL 4000EX	13	400	0.9	1.7	6	1.2	47	90	1.6
Cambridge HREM	12	600	2.5	2.7	8	1.0^h	69	131	1.7

[a] Objective lens aperture diameter, in reciprocal space units.
[b] Maximum operating energy.
[c] Data taken from M.A. O'Keefe, Ultramicroscopy 47 (1992) 282.
[d] Defocus value corresponding to the zeroth order passband (Scherzer defocus).
[e] Defocus value corresponding to the second order passband.
[f] CTF crossover at Scherzer defocus.
[g] Data estimated for the microscope at the University of Cadiz.
[h] Approximated values.

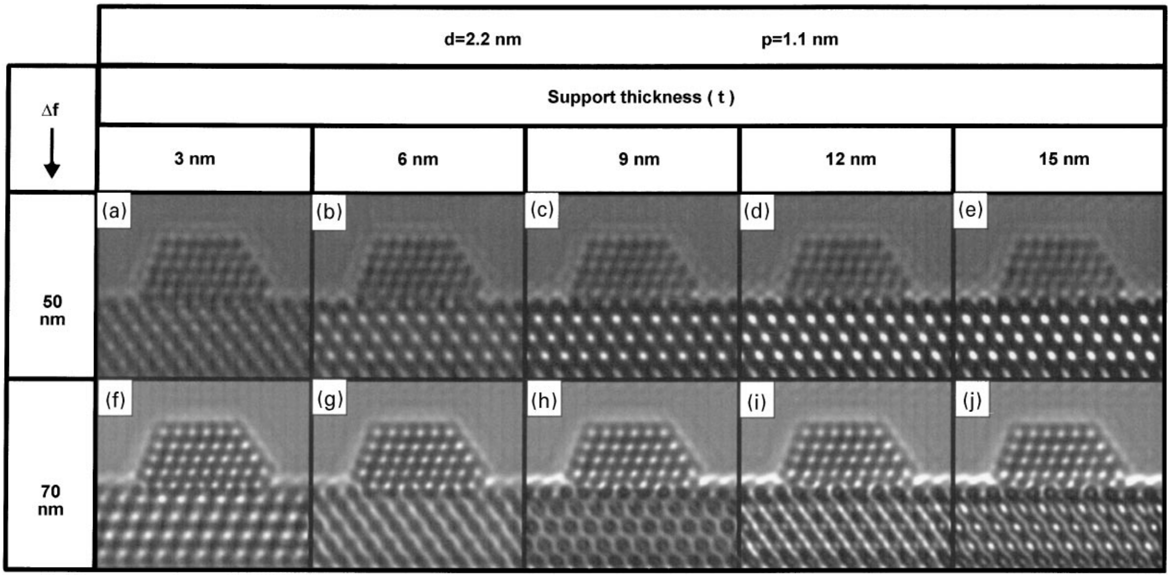

Fig. 8. Calculated images at 50 and 70 nm defocus taking into account the effect of changing support thickness between 3 and 15 nm. See text for details about the models used as inputs for these calculations.

particles. This is in good agreement with the result obtained in the previous section, where a negligible transfer of diffracted amplitude between the two components of the system and no alteration of the beams' phase with respect to the isolated components were detected. Note in this respect that in these models the metal particles are placed very close to the exit surface, so that no propagation of the metal beams within the support material occurs. Calculations based on thicker support crystals, about 70 nm, for which this propagation effect can take place did not show any significant modification in the contrasts of the metal in the regions away from the interface. The small amplitude modifications observed in the amplitude/phase diagrams of the metal particles supported on thick support crystals, Fig. 7, do not induce drastic changes in the metal particle contrasts.

Finally the results presented in this section indicate that the determination of t and Δf for the support can be done on the basis of thickness vs. defocus simulation maps calculated for this component alone, without considering the presence of a metal particle on its surface.

5.2. *Effect of particle position p*

To understand the role of this parameter the calculated images gathered in Fig. 10 should be analysed. These calculations correspond to structural models, shown in Fig. 11, containing a metal particle with the same features of those described in the previous section. In all cases the support thicknesses have been kept constant at a value of 12.5 nm and particle position parameters (p) with a value of 1.25 nm ($0.1t$) and 11.25 nm ($0.9t$) have been considered.

If images calculated for a given defocus are compared, it can be clearly observed that, as the position changes, the contrasts exhibited by the metal particle are modified. This result indicates that the effective defocus for the particle image is changing with its position and, on the other hand, that this effective defocus deviates from the nominal value.

A further comparative analysis of the images contained in Fig. 10 indicates that a 10 nm displacement on the support surface along the beam incidence direction is equivalent to a defocus increase of 10 nm. In effect, the image calculated for

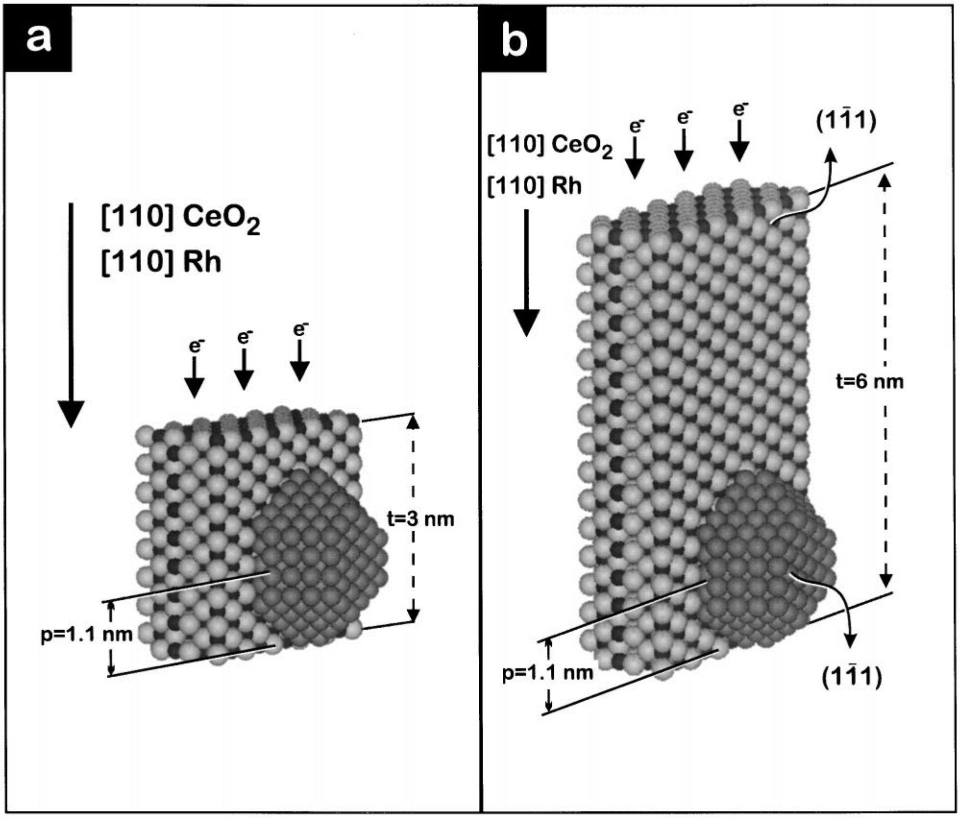

Fig. 9. Structural models corresponding to Rh/CeO$_2$ supercells containing a (1 $\bar{1}$ 1)-truncated cuboctahedron rhodium particle supported on a (1 $\bar{1}$ 1) surface of a ceria crystallite 3 nm (a) and 6 nm (b) thick. Note how the diameter of the metal particle and its position are the same in these two models.

$p = 11.25$ nm and $\Delta f = 50$ nm shows a particle whose contrasts match those observed for the image with $p = 1.25$ nm and $\Delta f = 60$ nm, a similar correlation existing between the pairs of images indicated by the white double arrows in Fig. 10. This result is, once more, in good agreement with the observations made on the basis of the amplitude/phase curves that predicted a change in the phase of the (1 $\bar{1}$ 1) beams of the metal particle as p was changed.

Using the well known expression for the phase shift introduced by instrumental aberrations [32], the change in phase shift, for a reflection of module g, associated to a change in the defocus value can be estimated according to the following equation,

$$\Delta\chi = \pi\lambda g^2 \Delta(\Delta f) \tag{11}$$

That, by using Eq. (8), can be rewritten as

$$\Delta\chi = R_\phi \Delta(\Delta f). \tag{12}$$

Keeping in mind that the term Δ_χ represents a change in the phase shift between the diffracted and the unscattered electron beam, the comparison of Eqs. (10) and (12) indicates, as the former calculations clearly demonstrated, that a displacement of the metal particle on the surface of the support material is equivalent to a change of the defocus of the same magnitude.

The results commented on above point out that for the interpretation of one image of a supported metal catalyst two different defocus values have to be provided; that corresponding to the support, and the other that must be assigned to the metal particle. These two values will differ from each

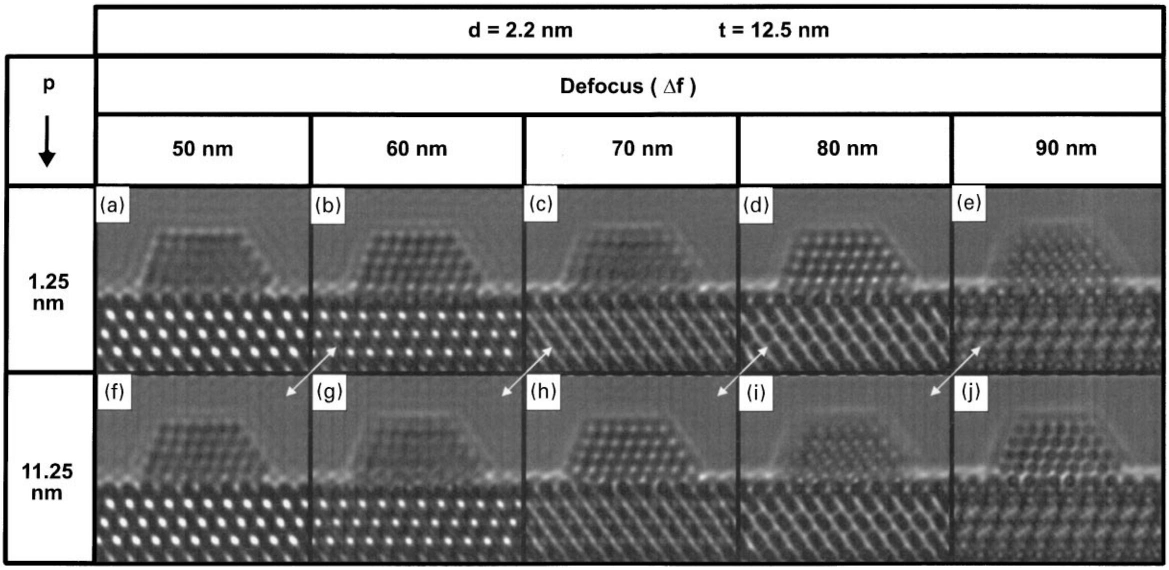

Fig. 10. Calculated images at 50 and 70 nm defocus taking into account the effect of changing the particle position on the support surface. See text for details about the models used as inputs for these calculations.

other, the amount of the difference being a function of the exact position of the metal particle on the surface of the support. This is a particular feature of HREM imaging of systems with spatially discrete interfaces, as is the case of supported metal catalysts, not applicable to the images of extended interface systems, where just one defocus setting is necessary to define their recording conditions. The relationship between the nominal, support, defocus and that corresponding to the metal particle can be expressed according to the following equation:

$$(\Delta f)_{\mathrm{metal}} = (\Delta f)_{\mathrm{support}} - p. \qquad (13)$$

5.3. *Effect of particle size d*

$(1\,\bar{1}\,1)$-Truncated cuboctahedron shaped rhodium particles with diameters ranging, roughly, from 0.5 nm up to 1.5 nm (in a number of atoms base from 1 to 133 atoms) have been modelled for these calculations, Fig. 12. In all cases these particles have been grown on a $(1\,\bar{1}\,1)$ surface of a ceria crystallite of 9 nm thickness and in a parallel topotaxy. In the calculated images, Fig. 13, both components are imaged down their [1 1 0] zone axis. Calculations were done at nominal defocus values, support defocus, of 50 and 70 nm.

According to this figure, particles with a number of atoms down to 45 can be clearly identified in the images and distinguished from the contrasts due to the support surface. The faint contrasts observed for the particle consisting of 28 atoms could still be assigned to a rhodium metal phase, on the basis of digital intensity profiles recorded along the $[\bar{1}\,1\,2]$ direction, but could be ascribed to surface inhomogeneities of the support on the grounds of a naked eye inspection. Finally, calculated images indicate that isolated metal atoms can not be distinguished on the surface of ceria in profile view images. In effect, image Fig. 13a has no information about the position of the metal atom, that was positioned at the centre of the surface in the model used for the calculation, Fig. 12a.

A second aspect worth mentioning with regard to Figs. 12 and 13 is that related to the comparison of the apparent size of the HREM image of the metal particle and the real size of the modelled particle. In effect, O'Keefe et al. [10] have reported

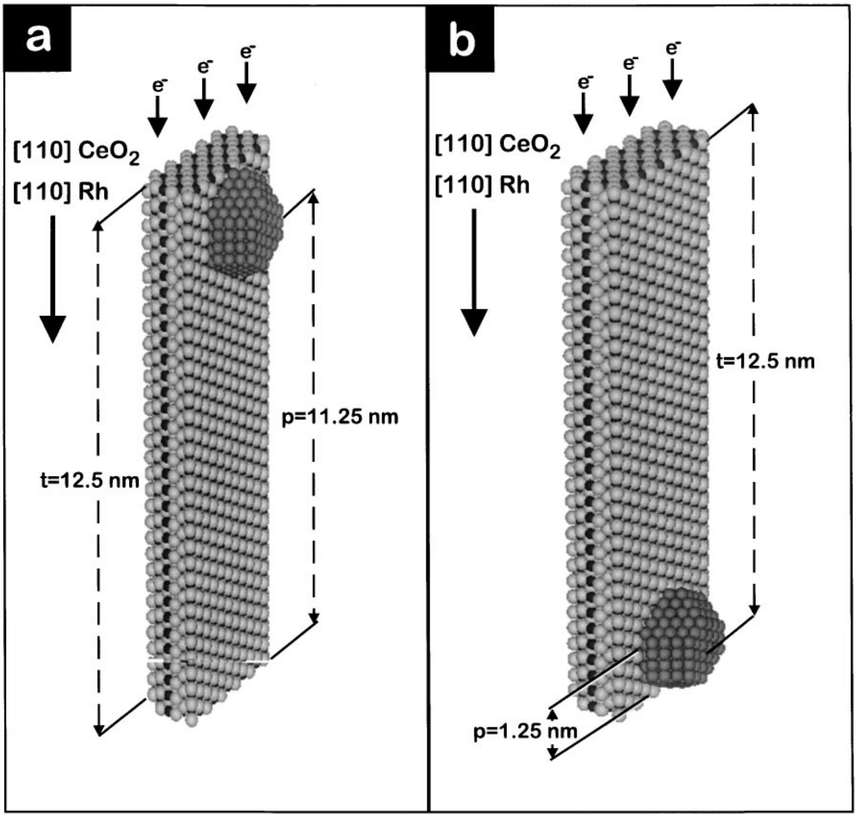

Fig. 11. Structural models corresponding to Rh/CeO$_2$ supercells containing a $(1\,\bar{1}\,1)$-truncated cuboctahedron rhodium particle supported on a $(1\,\bar{1}\,1)$ surface of a ceria crystallite 12.5 nm. In (a) the particle is positioned at the entrance of the model while in (b) it is close to the exit surface. Note how the diameter of the metal particle and support thickness are the same in these two models.

the occurrence of discrepancies between real and apparent particle size due to Fresnel contrast effects at the surface of small metal clusters. According to these authors, apparent surface relaxation takes place mainly at thick edges, the effect being sensitive to imaging conditions, mainly to the defocus setting. Moreover, taking into account that metal clusters are shaped, for a given defocus these distortions are direction dependent, this giving rise to modifications in the aspect ratio of the particles [10]. In the simulations herein considered, in the range corresponding to easily detectable particles, these distortions are very small, actually lower than the usual experimental error associated with the measurement of metal particle size. The distortions are even smaller when working close to the Scherzer defocus, Figs. 13a–13e, in good agreement with the results reported by O'Keefe et al. [10].

The Fresnel diffraction effects commented on above are also responsible of the 'ghost' fringes observed in most of the simulated images at the free space surrounding the metal particles or the support. The visibility of such fringes depend both on the imaging conditions and on the electronoptical parameters, mainly those related to the coherence of the electron beam, employed for the calculations. In general these fringes are most easily seen on calculated than on experimental recordings. The overestimation of the electron source coherence parameters and the absence of noise in the calculated images contribute to create this difference.

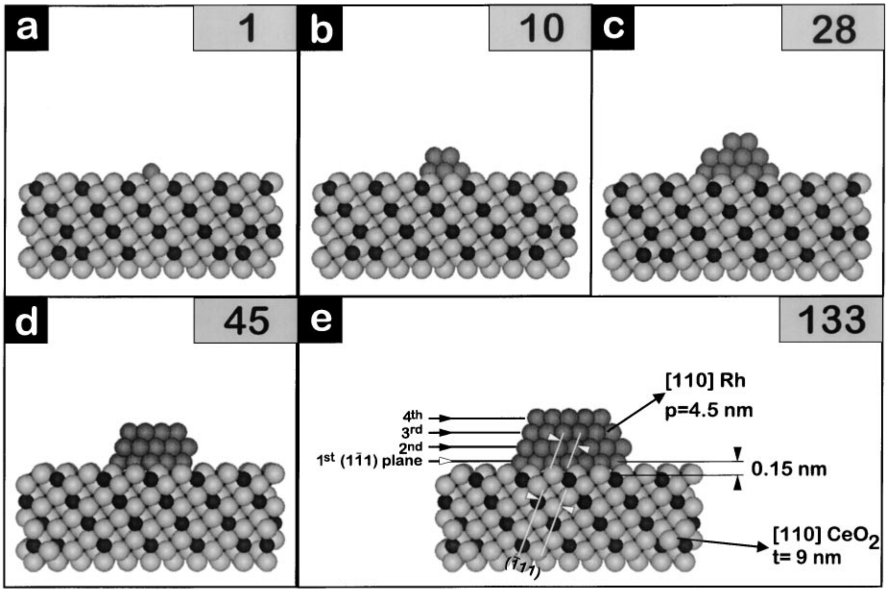

Fig. 12. Structural models corresponding to Rh/CeO$_2$ supercells containing (1 $\bar{1}$ 1)-truncated cuboctahedron rhodium particles with increasing size. The number of atoms in each particle has been marked at the upright corner of each figure. In this case the position of the metal particle and the support thickness have been kept constant in the different models; $t = 9$ nm and $p = 4.5$ nm.

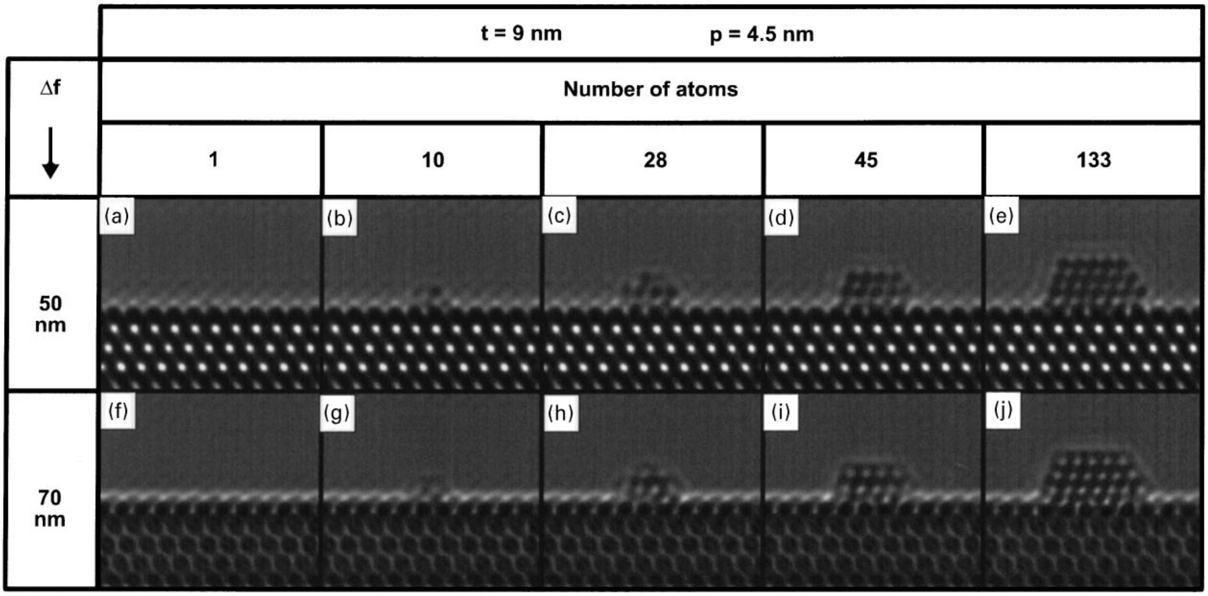

Fig. 13. Images calculated at 50 and 70 nm defocus for the different supercells contained in Fig. 12. The electronoptical parameters characteristic of a JEOL 2000EX have been used for these calculations.

A second question that represents a problem in determining the particle size in the HREM image is the possibility of detecting the first $(1\,\bar{1}\,1)$ plane of metal atoms in direct contact with the support surface, that marked with a white arrow in Fig. 12e. In this respect, it can be noted, by comparison of the models contained in Fig. 12 with the simulated images of Fig. 13, that the visibility of the first rhodium atom layer is more limited at 50 nm defocus than at 70 nm; at least for the support thicknesses considered in these simulations. In effect, the white contrast type obtained for 70 nm defocus allows to distinguish more clearly this layer in Figs. 13f–13j than in Figs. 13a–13e where the black dot contrasts are nearly buried within those due to the support surface. If we recall the results of Section 5.1, dealing with the effect of thickness, it is reasonable to expect that the defocus value showing optimum visibility of the first layer stays close to 70 nm for different support thicknesses. This idea is confirmed by the simulations contained in Fig. 8 where, in general, all the images show a neat row of white dots close to the support surface. Though for thick crystals, Fig. 8e, some distortions are already evident in this row of white dots, their visibility improves, in any case, when compared to the images calculated at a defocus of 50 nm.

The possibility of imaging the first metal atom layer will play a more important role in the determination of real particle size than the apparent relaxation effects due to Fresnel effects observed in isolated particles. In any case, the error induced by the former effect will never be greater, in the worst of cases, than one interplanar spacing, a $\{1\,1\,1\}$ *d*-spacing in our models. This amounts to about 0.22 nm, a value that is of the order of magnitude of the experimental error associated to the measurement of particle size by any means.

In summary the apparent size that can be measured on experimental HREM images corresponds, very closely, to the real particle size, even more when dealing with particles with sizes over 1 nm. At least, specific experimental imaging conditions can be employed for which the differences between real and apparent sizes can be minimised. In the worst of cases, for a given set of recording conditions, deviations larger than a few percent should not be expected for such size range, which, on the other

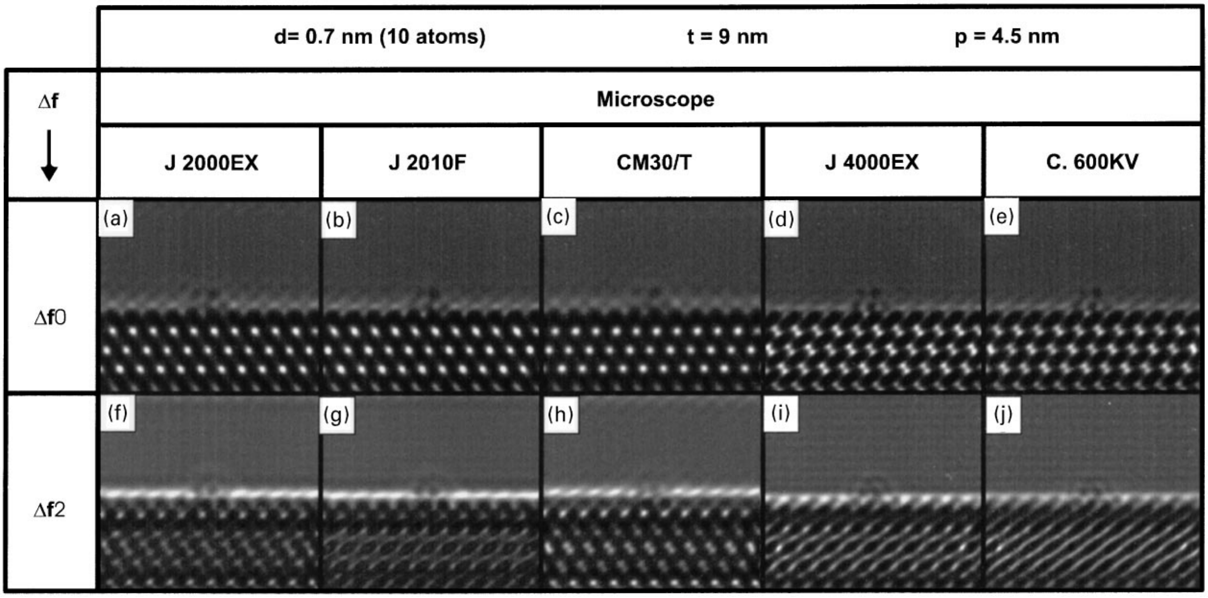

Fig. 14. Images calculated at the 0th (Δf_0) and 2nd (Δf_2) order passbands of different electron microscopes for the model shown in Fig. 12b.

hand, should not cause any problem given the usual experimental accuracy with which particle size is measured.

A final question that has been addressed using image simulation is the possible extension of the visibility to lower rhodium particle sizes that could be attained using electron microscopes with improved point to point resolution. Fig. 14 shows a set of calculated images of the Rh/CeO_2 supercell of Fig. 12b, i.e. a 10 atom rhodium particle supported on a ceria crystallite of 9 nm, for different electron microscopes with varying structural resolution values. For comparison purposes, the images corresponding to the defocus values giving rise to the zeroth and second order passbands have been calculated for each of the selected microscopes. These defocus values were estimated, as described in Ref. [32], using

$$\Delta f_n = [(4n+3)/2)]^{1/2}(C_s\lambda)^{1/2} \quad n = 0,2. \tag{14}$$

Data included in Table 1 were also used as input parameters for the calculations gathered in Fig. 14. The particle size employed in these calculations corresponds to the limit of detection in the JEOL2000EX. In fact in Fig. 14a the metal particle cannot be clearly distinguished from support surface contrasts.

A very slight improvement in the visibility of the metal cluster is obtained for the JEOL-2010F or the CM30. The best results are obtained in the JEOL-4000EX or Cambridge 600 kV ARM. For the last two microscopes the point to point resolution is closer to 0.15 nm, the distance established in the model of Fig. 12e between Rh and ceria at the interface. This allows, very likely, the improvement of the visibility of the first metal atom layer, a key point in this case to recognise the presence of such a small metal particle on the surface of ceria. According to images contained in Fig. 14, the defocus corresponding to the 0th order pass band, seems better to image this small cluster, in comparison with the 2nd pass band defocus value for which the white atomic column contrasts are more difficult to observe.

The results commented on above show that image calculation can be used to provide an answer, at least at a semiquantitative level, to the question of the visibility limit of small clusters in profile view imaging, for a given instrument, and set up a reasonable value of the lowest detectable size in this particular type of images. In this work a specific orientation for the metal and the support have been considered just as an example of what can be done with respect to this topic using image simulation, but it is clear that, using adequate modelling tools such as the RHODIUS program, very different experimental conditions can be analysed. Such extensive work is out of the scope of this contribution but the information that could be drawn from this analysis have to be considered of high interest in order to know, on an objective basis, the limitations of HREM when applied to supported metal catalysts. The results of such a study should also be taken into account when interpreting data of particle size distributions generated from HREM micrographs of real metal/support catalysts.

The relevance of the results here presented in relation to the effect of particle size, is made clearer if we recall that the estimation of metal particle size distributions is the information most often, even routinely, drawn in the literature from the EM analysis of catalytic samples.

6. The effect of crystal tilt in HREM imaging of supported metal catalysts

Supported metal catalysts, as most heterogeneous catalysts, are powder materials constituted of ensembles of randomly oriented microcrystals aggregated to a greater or lesser extent. In such conditions, a superposition in the diffraction plane of information coming from neighbouring microcrystals is, in practical terms, unavoidable. On the basis of such multiple diffraction patterns the operation of the microscope goniometer to get a fully in-zone orientation for one of these microcrystals is not an easy task. For this reason, it is usual that HREM recordings on these polymicrocrystalline materials contain residual tilt effects.

The influence of crystal tilt on HREM images of crystalline specimens has been widely discussed in the literature [33–36] on the basis of both experimental and calculated images. In Refs. [35,36], O'Keefe et al. point out the problems in determining crystal thickness by using an experimental to simulated image matching procedure, which arise because of very slight crystal tilts. Similar simulation studies concerning the effect of tilt on HREM images of isolated small metal particles with different crystallographic structures have also been reported [10,14,37].

Crystal thickness determination is a particularly complex problem in polymicrocrystalline materials that is further complicated because of tilting as suggested in Refs. [35,36]. This topic will not be discussed here, instead we will focus our attention on the role of this problematic parameter on both the resolution and, what is more interesting, on the incorporation of artefacts in HREM images of metal/support systems not related to the real structure of the catalyst.

Fig. 15 shows a sequence of simulated images at the same nominal support defoci, Δf: 50 or 70 nm, where tilts of increasing magnitude, from 0° to 7°, around an axis perpendicular to the $Rh\|CeO_2$ interface plane, axis numbered as **1** in Fig. 16, have been considered. A rhodium particle with a diameter close to 2 nm sitting on a $(1\,\bar{1}\,1)$ surface of a 9 nm thick ceria crystallite, both in [1 1 0] orientation, have been modelled for this calculation. Note that in this case the main visible effect associated to tilting consists in a loss of structural resolution in the HREM image that affects both the metal particle and the support crystallite. A continuous transition from dot to fringe-like images is observed as the tilting angle increases. The threshold value of the tilting angle necessary to reach the fringe pattern image can be defined using these calculations for both the metal particle and the support. Given its smaller size this value is lower for the last, as could reasonably be expected. In effect, a tilting angle of 3°, Figs. 15c and 15h, gives rises to a $\{1\,1\,1\}$ fringe image of CeO_2 while for this same tilting angle the image of the rhodium particle still exhibits bidimensional resolution. It is necessary to increase the tilting angle up to 7°, Figs. 15e–15j, in order to obtain a $\{1\,1\,1\}$-fringe image of the metal particle. For higher tilting angles images similar to those in Figs. 15e and 15j are observed.

To obtain the calculated images shown in Fig. 15 a rhodium particle grown on ceria according to a parallel topotaxy orientation relationship was considered, but similar results are obtained for

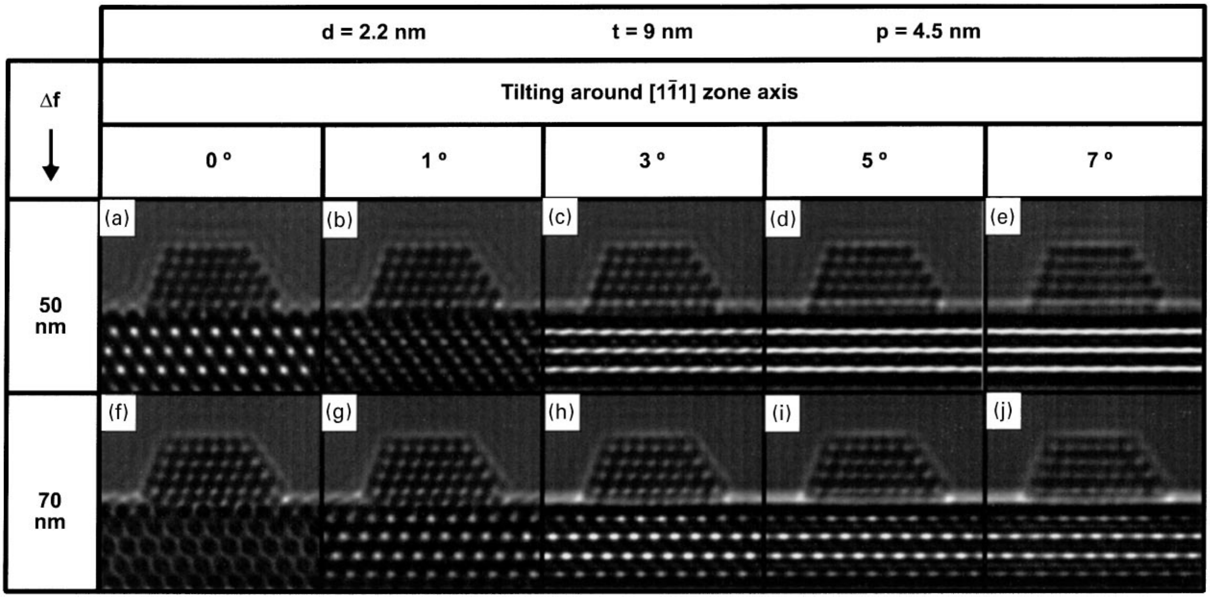

Fig. 15. Image calculations, at 50 and 70 nm defocus, showing the effect of crystal tilts around the $[1\,\bar{1}\,1]$ axis of CeO_2. Tilt angle is marked over each image. The Rh/CeO_2 supercell employed for these calculations consisted of a rhodium particle like that in Fig. 9 sitting on the $(1\,\bar{1}\,1)$ surface of a 9 nm thick ceria crystal under parallel topotaxy. The value of p for the particle was 4.5 nm.

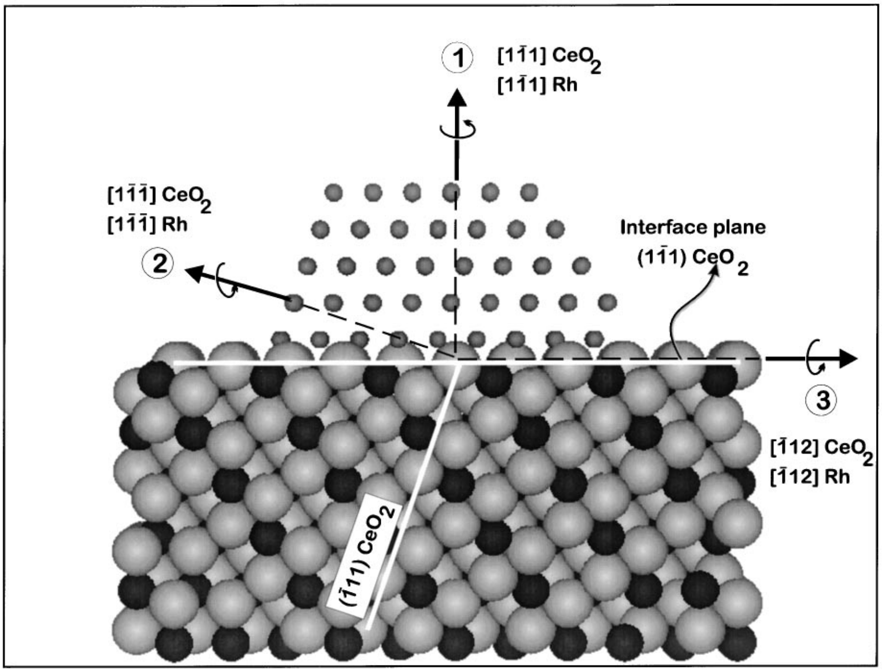

Fig. 16. Model of a Rh/CeO_2 supercell depicting the geometry of the different tilt axis employed in the evaluation of tilt effects in supported metal catalysts.

other orientation relationships, as it could be the case of a twin topotaxy.

HREM images similar to those shown in Fig. 15 are commonly recorded in practice. Fig. 17a shows an experimental example where a crystal tilt around a $(1\,\bar{1}\,1)$ axis is present. The parallel alignment of $\{1\,1\,1\}$ fringes of metal and support is evident and reveals the existence of specific metal/support orientation relationships like those considered in the models of Fig. 16. The calculated image shown in Fig. 17b reproduces quite well this effect and other striking contrast features observed in the experimental image like the thinning of the uppermost (1 1 1) black fringe beneath the metal particle. This detail can be most easily noticed if the experimental or simulated images are seen in glancing angle in the direction of the fringes. The thinning effect is not due to tilting but to the presence of the metal particle on the surface, because it can also be observed in calculated images corresponding to models where both the metal and the support are imaged in the exact [1 1 0] zone axis, see previous figures. The appearance of 'V' shaped contrasts at the bottom right corner of the contact region between the fringes of the metal and the support, marked with arrows in Fig. 17a, is also clearly visible in the calculated image. Though this effect will be discussed in more detail below it is important to note here that it is related both to tilting and to the presence of an extra (1 1 1) ceria plane on the right side of the metal particle. In fact, the metal particle has been grown in the model close to a surface step, Fig. 17c. This surface step consists of a $(1\,\bar{1}\,1)$ plane of one atomic layer height, Fig. 17d.

A second geometry of tilt that deserves some attention is that involving a tilt axis not perpendicular to the Metal$\|$Support interface plane. Fig. 18 shows the calculations corresponding to models of a Rh particle, grown in parallel topotaxy on ceria, where the whole supercell has been tilted around one such axis. Specifically the tilt axis was

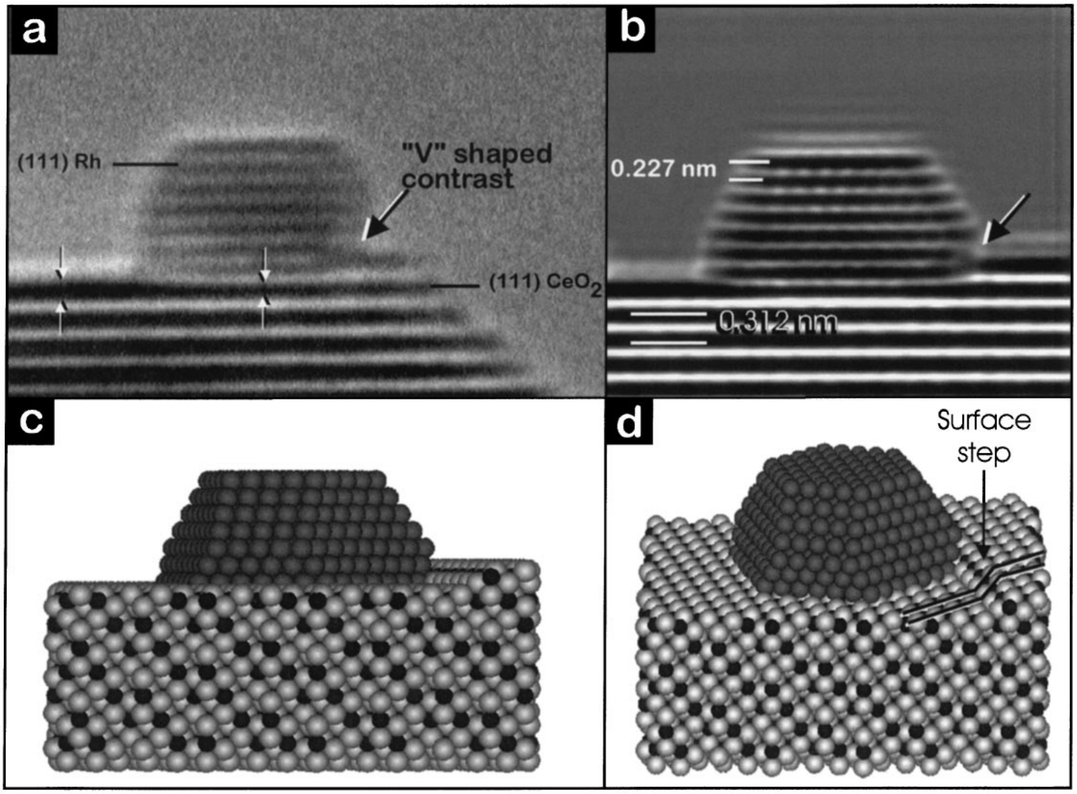

Fig. 17. (a) Experimental HREM image recorded on a 4% Pt/ CeO_2 catalyst and containing $[1\,\bar{1}\,1]$ tilt effects; (b) simulated image reproducing the contrasts shown in (a); (c) projection and (d) perspective views of the model employed to obtain the calculation shown in (b).

perpendicular to the set of $(\bar{1}\,1\,1)$ planes which lie oblique to the support surface, axis labelled as **2** in Fig. 16.

In this case, in addition to the loss of resolution detected in the previous example, some additional features of interest can be noted at the Metal||Support interface. Thus, in the images calculated for tilts of 5° and 7° clear distortions in the (1 1 1) metal fringes can be observed in the region of the image close to the interface. Bending of these fringes and propagation within the support fringes can be clearly observed. These distortions are most evident for the 7° tilted model where they give rise to 'V' and 'W' shaped contrasts easily detectable by direct inspection of images in Fig. 18e or Fig. 18j.

On the basis of a direct, naked eye, image interpretation procedure such distortions could be assigned to displacements in the metal atom positions in the regions close to the interface. The structural match between the metal and support planes contacting at the interface could be even suggested as the driving force for such displacements. However, if we recall that in the models employed for the calculations contained in Fig. 18, no distortion at the metal particle structure has been introduced, it is clear that this would be an example of a wrong interpretation. These results show the importance of image calculation and warn us about the problems that may arise when the fine details of the image contrasts of these materials are interpreted directly.

Fig. 19a shows an experimental image recorded on a Rh/CeO_2 catalyst where the metal particle shows the distorted fringes commented on above.

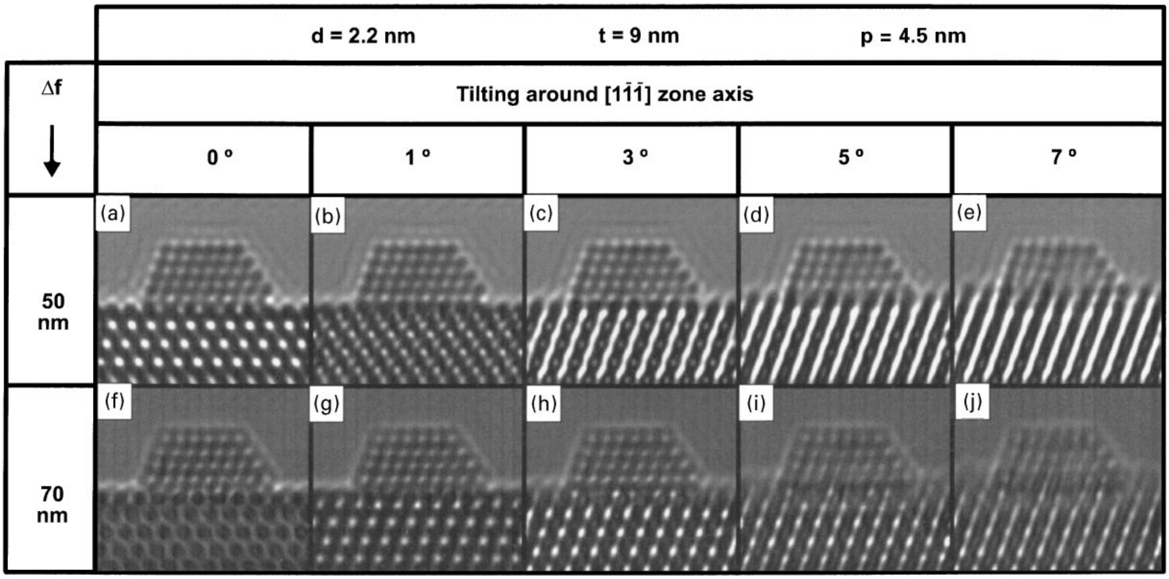

Fig. 18. Image calculations, at 50 and 70 nm defocus, showing the effect of crystal tilts around the $[1\ \bar{1}\ \bar{1}]$ axis of CeO_2. Tilt angle is marked over each image. The model employed to obtain the simulations included in Fig. 15 was also used for these calculations.

The calculations here presented indicate that this metal particle should not necessarily be strained. At least no displacements in the metal atom positions are needed in order to explain the striking contrasts observed at this $Rh\|CeO_2$ interface. To confirm this idea the Rh/CeO_2 supercell shown, in projection and perspective views respectively, in Fig. 19c and d was built. The model contains a non-distorted rhodium particle grown under parallel topotaxy and placed at 2.5 nm from the exit surface of a 5 nm thick ceria crystallite. The whole metal/support system was tilted 12° out of the [1 1 0] zone by using the $[\bar{1}\ 1\ 1]$ as tilting axis. The morphology of the metal particle, that was properly adjusted to fit the experimental image, can be clearly visualised in Fig. 19d. A very good agreement can be noted between the calculated and the experimental image allowing confirmation, as already stated, that no distortion of the rhodium structure needs to be taken into account to explain the contrasts observed in Fig. 19a. Some other aspects of this experimental image are worth mentioning, such as the wavy appearance of the support surface. This would suggest, once more on the basis of a direct interpretation, a non-flat support surface. This effect is also observed in the calculated image. If we observe, Fig. 19d, that the (1 1 1) surface employed in the model is atomically flat, it can be concluded that the roughness of the surface seen in the experimental image can be, at least partially, another imaging artefact. In fact the model shown in projection, Fig. 19c, shows the support surface with this rough aspect.

Finally the effect of tilting around an axis contained in the Metal||Support interface will be considered. This is the case of the axis marked as **3** in Fig. 16, the $[\bar{1}\ 1\ 2]$ axis of rhodium or ceria in this case. Figs. 20 and 21 contain different simulated images corresponding to the same model employed in previous cases but tilted around the $[\bar{1}\ 1\ 2]$ axis. In the case of Fig. 20 the metal particle was located close to the entrance surface of the model, $p = 7.2$, while in Fig. 21 the particle was placed close to the exit surface, $p = 1.8$. In this way the influence of particle position on tilting can be discussed by comparing the results of both figures. On the other hand, given that both positive and negative values have been considered in these

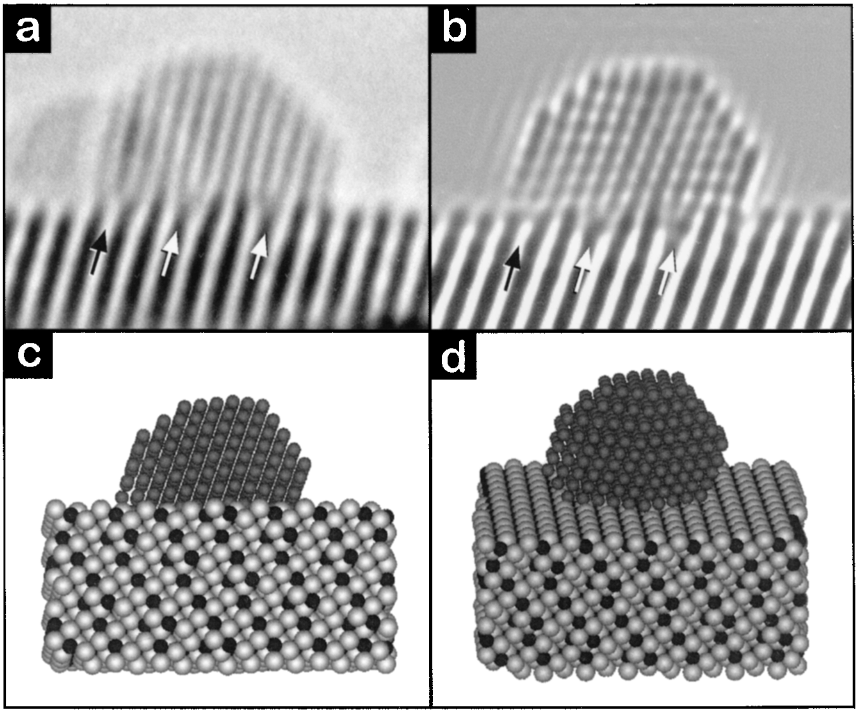

Fig. 19. (a) Experimental HREM image recorded on a 2.5% Rh/ CeO_2 catalysts and containing [1 $\bar{1}$ $\bar{1}$] tilt effects; (b) simulated image reproducing the contrasts shown in (a); (c) projection and (d) perspective views of the model employed to obtain the calculation shown in (b). The arrows in (a) and (b) indicate the approximate positions of the 'V', 'W' distorsion contrasts referred in the text.

calculations, the influence of the tilting sense, clock or anticlockwise, can also be addressed by analysing these figures.

Focusing first on the contrasts observed in the support, strong modifications are observed as a consequence of even low amplitude tilts, 1°. The sign of tilting makes in this case no difference, the images showing a trend to change from dot type to {1 1 1}-fringe type. On the other hand, particle position does not affect at all the contrasts observed in the support. A bending effect at the surface of the support can also be clearly observed in the ($\bar{1}$ 1 1) fringes of the images corresponding to the highest tilting angle, ± 3°. A sudden change in the direction of these fringes into a direction perpendicular to the surface plane, that affects the support region very close to this surface can be easily noted by direct inspection. This bending effect is an artefact related to tilting and not a consequence of real structural modifications.

With respect to the metal particle, a curious effect can be noted in the set of simulated images shown in these figures. This refers to the vanishing of one (1 1 1) atomic plane in the case of the images corresponding to ± 3° tiltings. Depending on the position of the metal particle, at the entrance or the exit surface, this effect is observed for positive or negative tilting respectively. Thus in Fig. 20h, the non-tilted particle, a total of five (1 $\bar{1}$ 1) planes can be counted in the metal particle. After a tilt of either + 3°, in the case of the particle placed at the entrance surface, Fig. 20e, or − 3°, in the case of the particle at the exit surface, Fig. 21a, only four (1 $\bar{1}$ 1) atomic planes can be summed up. This atomic plane burial effect is once more a new type of image artefact that can, in this case, change the apparent dimensions of the metal particle in a particular direction. Therefore these calculations indicate that some care should be taken when measuring particle size from HREM images

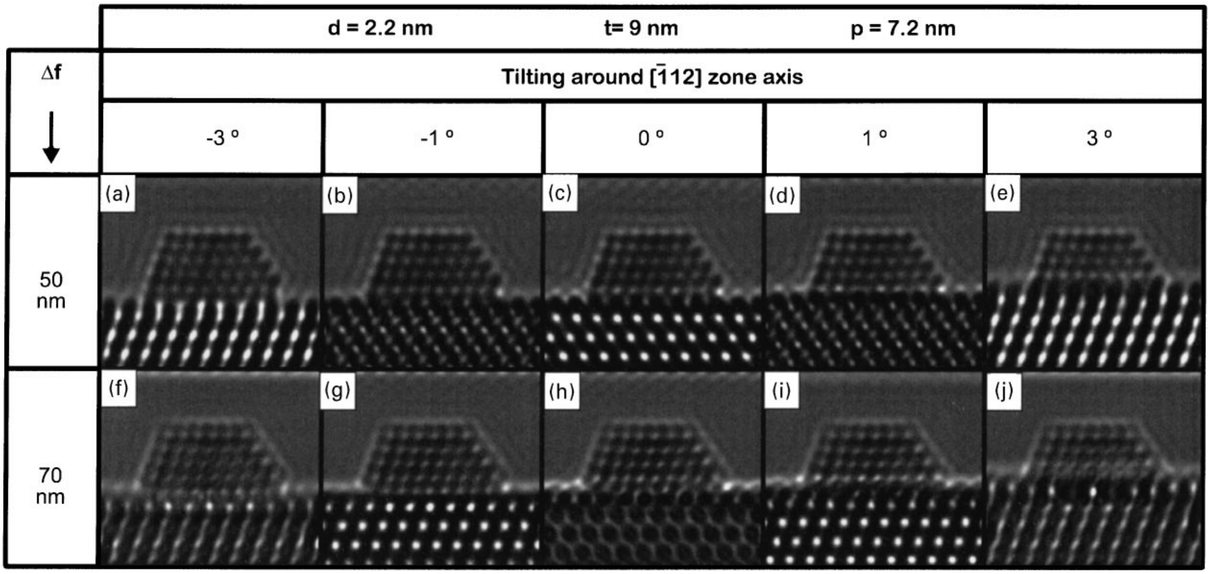

Fig. 20. Image calculations, at 50 and 70 nm defocus, showing the effect of crystal tilts around the [$\bar{1}$ 1 2] axis of CeO_2. Tilt angle is marked over each image. The metal particle is positioned at 7.2 nm from the supercell exit surface.

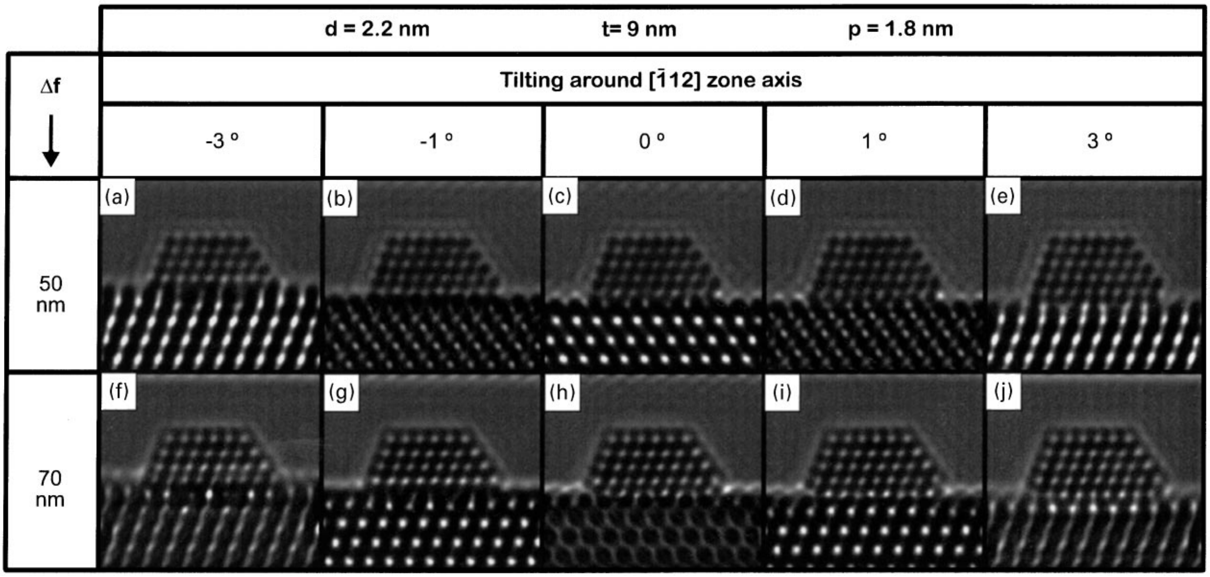

Fig. 21. The same as Fig. 20 but with a particle located at 1.8 nm from the exit surface.

of these materials, specially in the case of tilted images.

Fig. 22a contains an experimental HREM image recorded on a Pt/CeO_2 system where a tilt around the [$\bar{1}$ 1 2] axis is present. The calculated image shown in Fig. 22b matches fairly well the general contrast features present in the experimental recording. As depicted in Fig. 22c this calculation

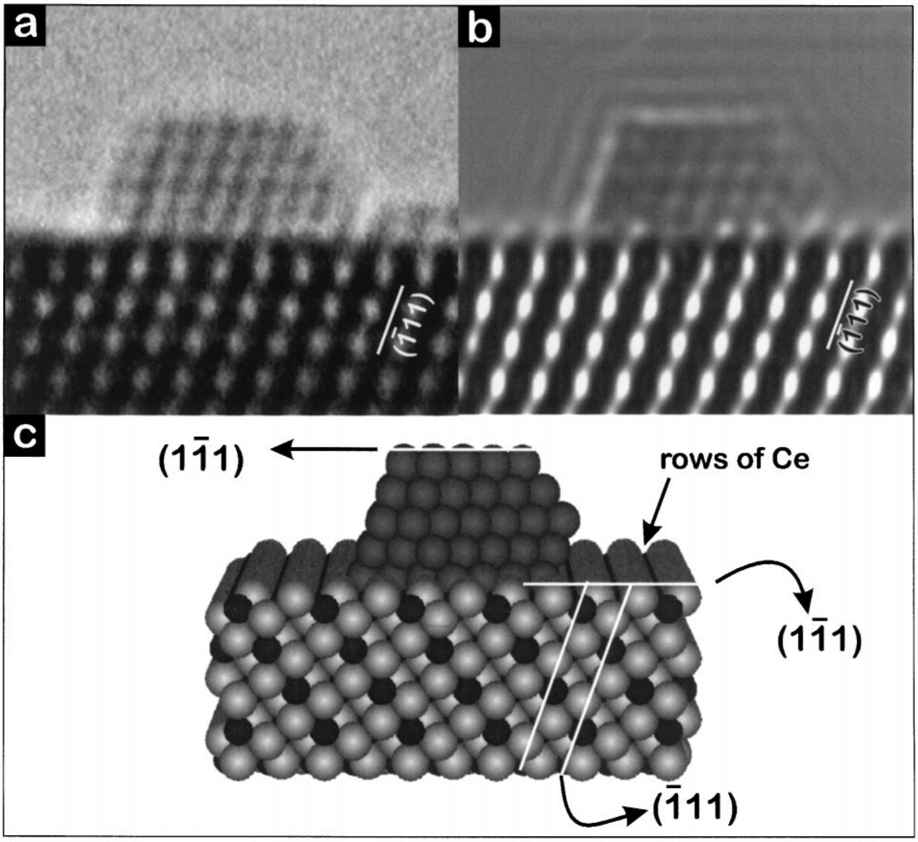

Fig. 22. (a) Experimental HREM image recorded on a 4% Pt/CeO_2 catalyst and containing [$\bar{1}$ 1 2] tilt effects; (b) simulated image reproducing the contrasts shown in (a); (c) perspective view of the model employed to obtain the calculation shown in (b).

corresponds to a (1 $\bar{1}$ 1) truncated cuboctahedron rhodium particle sitting on a (1 $\bar{1}$ 1) surface of a ceria crystallite with a thickness of 9 nm, the metal particle being at a distance, *p*, of 2 nm from the exit surface. The whole metal/support supercell was tilted 1.5° out of the [1 1 0] zone axis using as tilting axis the [$\bar{1}$ 1 2] direction of either rhodium or ceria given that a parallel orientation relationship was considered for the model. Fig. 22c suggests that the change in the orientation of the (1 $\bar{1}$ 1) fringes reported previously in the calculations included in Figs. 21a and 21e, may be due to the rows of closely spaced Ce atom brought out to the surface as a consequence of tilting. Such rows have been pointed out in Fig. 22c.

To summarise the results contained in this section, the calculations collected in Figs. 15–22 point out some of the problems that may arise when relying on a direct interpretation of the fine details of images recorded on metal/support systems out of the exact zone axis. It should be emphasised at this moment that, as stated at the beginning, this is the most common situation due to the usual experimental limitations.

7. Interpretation of experimental images

Finally this section is devoted, as an application example, to the interpretation of two different experimental HREM images recorded on M/CeO_2 catalysts. The first, Fig. 23a was recorded on a Rh/CeO_2 system that was treated in flowing hydrogen at 773 K and afterwards oxidised in pure

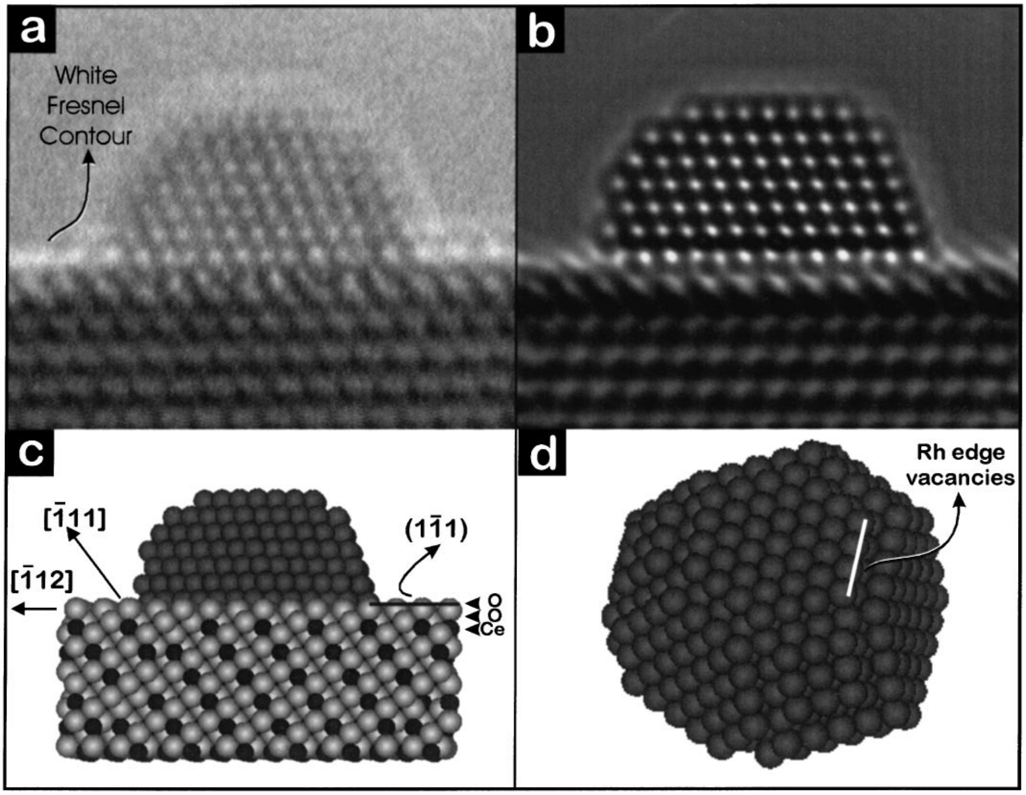

Fig. 23. (a) Experimental image recorded on a 2.5% Rh/CeO_2 catalyst reduced in hydrogen at 773 K and further oxidised at 373 K; (b) calculated image reproducing the main contrast features observed in (a); (c) projection view of the model employed to obtain calculation shown in (b). Note in this case the twin relationship between rhodium and CeO_2 and the presence of a double oxygen layer at the ceria surface; (d) structural model showing the details of the metal particle morphology. Note that in this case the rhodium particle contains atom vacancies along the different {1 1 0} edges of the (1 $\bar{1}$ 1)-truncated cuboctahedron.

flowing oxygen at 373 K. The main contrast features that deserve some attention in this experimental recording are the following: (a) the presence in the support of ($\bar{1}$ 1 1) planes containing dots elongated along the [$\bar{1}$ 1 2] direction; (b) anomalous surface contrasts, both on the free surface and beneath the metal particle. Specifically, an elongation along the [$\bar{1}$ 1 1] direction of the surface dots is evident. This change in the elongation direction with respect to the bulk contrasts results in an apparently zigzagged surface; (c) a clear white Fresnel contour at the support surface which crosses the region of the metal particle through its first (1 $\bar{1}$ 1) plane; (d) a white dot atomic column contrast in the metal particle and, finally, (e) a lower average intensity in the support region than in the metal particle region.

To reproduce all the features listed in the last paragraph a large number of structural models were built and their corresponding HREM images calculated. Between the parameters related to the structure the following were taken into account in these trials: support thickness, chemical features of the (1 1 1) surface, metal-support orientation relationship, metal particle shape and position and tilt along different axis. From this set, the most difficult to fix were the type and amplitude of tilts, the support thickness and the type of atomic termination for the surface. With respect to the latter, three different possibilities arise: a (1 $\bar{1}$ 1) surface with an oxide layer termination; a termination in Ce^{4+} cations and, the third case, a double oxide layer $(1\,\bar{1}\,1)$ surface. The selection of one of these three types of surfaces was further complicated by the fact that the surface contrasts depend strongly on tilting and support thickness, the other undetermined parameters in this case.

Fig. 23b shows the calculated image that, from the whole set of calculations carried out, best matched the experimental one. As depicted in Fig. 23c, this image can be interpreted in terms of a model containing a metal particle of rhodium of about 3.1 nm diameter supported on a ceria crystallite with a thickness of 9 nm. The orientation relationship between metal and ceria is that corresponding to a twin topotaxy. Both metal and support were tilted out of their [1 1 0] zone axis. A 3° rotation around the $[1\,\bar{1}\,1]$ axis of ceria followed, afterwards, by a 2° rotation around the $[\bar{1}\,1\,2]$ zone axis was performed for this purpose. The surface of ceria considered in the model corresponds to a double oxide layer termination. The last feature can be reasonably expected if we recall that the sample was submitted to an oxidation treatment at 373 K using pure oxygen. Let us recall also in this respect that some authors have detected the formation of surface peroxide species on ceria [38] during oxygen adsorption.

To improve the match in the case of the metal particle, a particular type of faceting was considered. This faceting, Fig. 23d, corresponds to a cuboctahedron truncated on a $(1\,\bar{1}\,1)$ plane, as

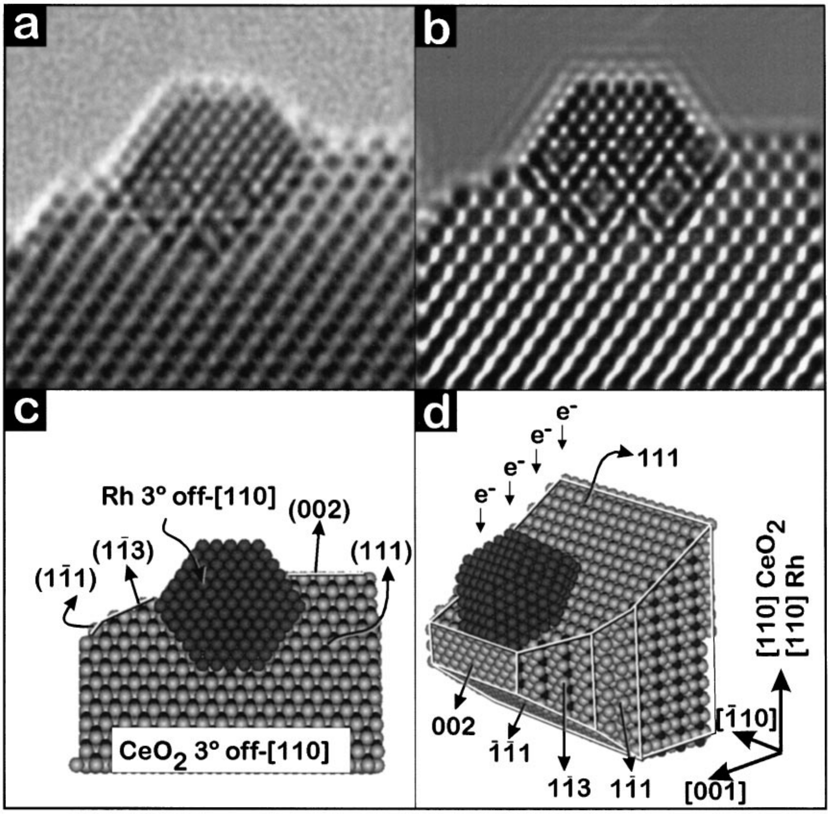

Fig. 24. (a) Experimental image recorded on a 4% Pt/CeO$_2$ catalyst reduced at 623 K; (b) calculated image reproducing the main contrast features observed in (a); (c) projection and (d) perspective views of the model employed to obtain the calculation shown in (b). Note in this case that both the metal and the support phases are shaped. Platinum is present as a $(1\,\bar{1}\,1)$-truncated cuboctahedron and ceria consists of a wedge crystal rounded by the planes whose Miller indices are pointed out.

already described in other cases, but with metal vacancies along the {1 1 0} type edges. To introduce these vacancies in the model, planes additional to those characteristic of the truncated cuboctahedron have to be considered within the faceting, that contained a total of 50 planes.

The contrasts observed in the calculated image corresponding to this model, Fig. 23b, match fairly well those contained in the experimental one and contain the different specific features listed in a previous paragraph.

Finally, Fig. 24a contains the second experimental image that will be considered in this section. In this case the micrograph was recorded on a Pt/CeO_2 catalyst treated in flowing hydrogen at 623 K. After performing image calculation on a number of structural models, the simulation shown in Fig. 24b was the one resembling most closely the contrasts observed in Fig. 24a. The model from which this calculation was obtained, Fig. 24c, introduces a new feature with respect to others presented in this paper, that is, a faceted support crystal. As drawn in Fig. 24d, the ceria crystallite consists in a wedge delimited by (0 0 2), $(\bar{1}\,\bar{1}\,1)$, $(1\,\bar{1}\,3)$ and $(1\,\bar{1}\,1)$ planes, in such a way that the crystal thickness changes from 6 nm in the thicker region down to 1.5 nm at the border, where the metal particle sits. This doubly faceted system, where both metal and support present a particular shape, can be properly modelled using the RHODIUS program developed in our lab and represents a situation often found in the field of HREM of supported metal catalysts. Regarding now the platinum, the metal particle presents a $(1\,\bar{1}\,1)$ truncated cubeoctahedron shape, with a diameter close to 3 nm. It was grown near the thin edge of the $(1\,\bar{1}\,1)$ exposed surface of the support crystal under a parallel topotaxy orientation relationship. The whole Pt/CeO_2 supercell was tilted 3° out of the [1 1 0] zone axis, using the $[1\,\bar{1}\,1]$ direction as tilting axis.

Note that a reasonable agreement has been obtained between the experimental and the calculated images. Thus, the change from a fringe to dot type contrasts observed in the $(\bar{1}\,1\,1)$ ceria planes when moving from the bulk to the surface has been reproduced in the calculated image. This feature results from the simultaneous action of tilt and thickness variation along the [0 0 1] direction. The shape and the contrasts observed within the metal particle are also close to those observed in the experimental image. Finally, if a closer observation of the experimental image is made, by viewing it in glancing incidence along the [0 0 1] direction, the presence of apparent bending contrasts at the Pt||ceria interface can be observed. Such contrasts, similar to those discussed in Figs. 17 and 18, are also present in the calculated image.

8. Conclusions

This paper describes the general guidelines to be followed to analyse the image contrasts obtained when studying multiphase catalytic systems by HREM. The examples used herein to illustrate the protocols and their capabilities, correspond to dispersed metal particles viewed on the edges of oxide support crystallites. However, most of the concepts and approaches considered in this contribution are also of interest as a ground to face also the interpretation of planar view HREM images of catalysts, and could be fruitfully applied to the study of many other complex nanostructured materials with discrete interfaces. Thus, the recording of HREM images, combined with its interpretation following image simulation approaches, is considered to be a powerful tool to understand the structural features which rely on many of the singular properties of this fast developing class of nanostructured materials, overcoming the inherent difficulties existing up to now for interpreting these results.

The procedure as a whole would follow the general trends well established for the interpretation of HREM images. First, it is necessary to build up the structural models representing the hypothetical nanostructures to be checked. To our knowledge there were no available software tools allowing to model, in a systematic, flexible and fine-controlled way, supercells describing multiphase systems with particles of variable shape, size, relative orientation and relative positions. That was in our view the major constrain to progress in the study of such complex systems. Secondly, the models are used to obtain simulated images: this task was carried out by using the multislice routines of the EMS package developed by P. Stadelman. The third point would be to evaluate the quality of the matching between the experimental images and the collection of simulated images, thus reaching a decision about the most likely interpretation and the degree of confidence in it.

Though we have not yet developed an original mathematical approach to compare the contrasts of experimental and calculated images for this type of materials, our experience in analysing very complex micrographs allows us to offer to the reader our view about the reliability of our interpretations.

First, it should be said that the process of mathematical comparison of simulations with images would be much more demanding, given the frequent complex features and large size of the supercells commonly used.

Second, the number of parameters considered in these simulations increases with the complexity of the model itself, and it could make an apparent good fitting suspicious of being fortuitous. Nevertheless, it should be considered that the number of features characteristic of an experimental image also increases very sharply with the complexity of the model. Thus, it is very difficult to reproduce the specific contrasts of the micrographs with simulated images of a structural model far apart from the reality. In conclusion, regardless of the most subtle details of the model, our experience points out to the difficulty of achieving acceptable fittings with erroneous models, and as a consequence to the reliability of our interpretations. This conclusion is also supported by our own experience and capabilities for simulation: as it is possible to simulate any imaginable situation, it is possible to know to what extent the gradual change in any of the parameters would introduce new image features or simply any other type of contrast variation.

An adequate training in using image simulation and supercell building software tools is a key factor to reach satisfactory results/effort outputs. The consideration of a broad number of parameters for the simulated images is also critical to get confidence in the adequacy of the best fitting models, as well as paying attention to the evolution of the simulated images with the gradual change of each parameter.

In any case, the point that we stress in this contribution is that the structural details which can be accessed by means of the simulation methodologies can be hardly achieved by the interpretation of results coming from any other experimental technique.

Acknowledgements

This work has been supported by the DGICYT (Project PB95-1257), the CICYT (Project MAT96-0931), and the Junta de Andalucía. The HREM images reported in this work were obtained at the Electron Microscopy Facilities of the University of Cadiz.

We also acknowledge specially Professors P. Stadelmann and P.A. Buffat, at the Ecole Polytechnique Federale de Lausanne (Switzerland), for introducing, training and continuously supporting some of us in the field of HREM image simulation.

References

[1] Special issue: HRTEM for Catalysis, Catal. Today 23 (3) (1995).
[2] Special issue: Electron Microscopy, Catal. Rev. Sci. Eng. 34 (1&2) (1992).
[3] Special issue: Characterization of Catalysts, Ultramicroscopy 34 (1&2) (1990).
[4] Special issue: Atomic Structure and Properties of Small Particles, Ultramicroscopy 20 (1&2) (1986).
[5] M.J. Yacaman, Appl. Catal. 13 (1984) 1.
[6] M.A. O'Keefe, P.R. Buseck, S. Iijima, Nature 274 (1978) 322.
[7] D.A. Jefferson, A.I. Kirkland, A. Reller, D. Tang, T.B. Williams, W. Zhou, Electron Microscopy 2 (1992) 611.
[8] D.A. Jefferson, Electron Microscopy 2A (1994) 341.
[9] S. Giorgio, C.H. Henry, C. Chapon, G. Nihoul, Electron Microscopy 2A (1994) 349.
[10] V. Radmilovic, M.A. O'Keefe, 53rd Ann. Proc. MSA, Kansas City, Missouri, 1995, p. 564.
[11] S. Giorgio, C. Chapon, C.R. Henry, Phil. Mag. A. 64 (1) (1991) 87.
[12] P.L. Gay, M.J. Goringe, J.C. Barry, J. Microscopy 142 (1) (1986) 9.
[13] M.J. Yacamán, G. Díaz, A. Gómez, Catal. Today 23 (3) (1995) 161.
[14] M. Flüeli, Thesis of the Ecole Polytechnique Federale de Lausanne, no. 796, Switzerland, 1989.

[15] P.A. Buffat, M. Flüeli, R. Spycher, P. Stadelmann, J.P. Borel, Faraday Discuss. 92 (1991) 173.

[16] J.V. Sanders, Ultramicroscopy 20 (1986) 33.

[17] P.L. Hansen, H. Topsøe, J.-O. Malm, Electron Microscopy 2B (1994) 1077.

[18] F.J. Botana, J.J. Calvino, G. Blanco, M. Marcos, J.A. Pérez-Omil, Electron Microscopy 2B (1994) 1085.

[19] P. Stadelmann, Ultramicroscopy 21 (1987) 131.

[20] S. Bernal, F.J. Botana, J.J. Calvino, C. López, J.A. Pérez-Omil, J.M. Rodríguez-Izquierdo, J. Chem. Soc. Faraday Trans. 92 (15) (1996) 2799.

[21] S. Bernal, F.J. Botana, J.J. Calvino, G.A. Cifredo, J.A. Pérez-Omil, J.M. Pintado, Catal. Today 23 (1995) 219.

[22] J.A. Pérez-Omil, Thesis of the Universidad de Cádiz, Spain, 1994.

[23] S. Bernal, F.J. Botana, J.J. Calvino, G.A. Cifredo, J.A. Pérez-Omil, Proc. EMAG'93. Inst. Phys. Conf. Serv. No. 138, Liverpool, UK, 1993, p. 485.

[24] S. Bernal, G. Blanco, J.J. Calvino, G.A. Cifredo, J.A. Pérez-Omil, J.M. Pintado, A. Varo, Stud. Surf. Sci. Catal. 82 (1994) 507.

[25] S. Bernal, J.J. Calvino, J.M. Gatica, C. Larese, C. López-Cartes, J.A. Pérez-Omil, J. Catal. 169 (1997) 510.

[26] S. Bernal, F.J. Botana, J.J. Calvino, J.A. Pérez-Omil, J.M. Rodríguez-Izquierdo, Book of Abstracts EUROPACAT-II, Maastricht, The Netherlands, 1995, p. 705.

[27] S. Bernal, J.J. Calvino, M.A. Cauqui, M.P. Corchado, J.A. Pérez-Omil, J.M. Pintado, Book of Abstracts 11th ICC, Baltimore, EEUU, 1996, PO-067.

[28] R.W. Glaisher, A.E.C. Spargo, D.J. Smith, Ultramicroscopy 27 (1989) 19.

[29] R.W. Glaisher, A.E.C. Spargo, D.J. Smith, Ultramicroscopy 27 (1989) 35.

[30] R.W. Glaisher, A.E.C. Spargo, D.J. Smith, Ultramicroscopy 27 (1989) 117.

[31] S. Giorgio, C. Henry, C. Chapon, J.M. Penisson, J. Crystal Growth 100 (1990) 254.

[32] J.C.H. Spence, Experimental High Resolution Electron Microscopy, Oxford University Press, Oxford, 1988, p. 106.

[33] P.G. Self, R.W. Glaisher, A.E.C. Spargo, Ultramicroscopy 18 (1985) 49.

[34] D.J. Smith, W.O. Saxton, M.A. O'Keefe, G.J. Wood, W.M. Stobbs, Ultramicroscopy 11 (1983) 263.

[35] M.A. O'Keefe, V. Radmilovic, 50th Ann. Proc. EMSA, Boston, MA, 1992, p. 116.

[36] M.A. O'Keefe, V. Radmilovic, 51st Ann. Proc. EMSA, Cincinatti, OH, 1993, p. 980.

[37] J.-O. Malm, M.A. O'Keefe, Proc. SCANDEM-93, Lund, Sweden, 1993, p. 131.

[38] J. Soria, A. Martínez-Arias, J.C. Conesa, G. Munuera, A.R. González-Elipe, Surf. Sci. 251/252 (1991) 290.